THE UNIVERSITY OF CHICAGO

MAPPING SODIUM IN SINGLE ORGANELLES IN VIVO

A DISSERTATION SUBMITTED TO

THE FACULTY OF THE DIVISION OF THE PHYSICAL SCIENCES

IN CANDIDACY FOR THE DEGREE OF

DOCTOR OF PHILOSOPHY

DEPARTMENT OF CHEMISTRY

BY

JUNYI ZOU

CHICAGO, ILLINOIS

MARCH 2023

Table of Contents

List of Figures

List of Tables

Acknowledgements

I would like to thank many people in this journal of graduate school. First, I want to thank my advisor, Yamuna Krishnan. Yamuna always tries to bring the best out of students. She is strict in making me think about science critically, which lays strong foundation as a researcher for me. She is also understanding and considerate outside of science. And I would not have started this project and taking risk at fourth year of Ph.D. without her motivating me. And I have learned a lot from Yamuna which will benefit me for a lifetime.

Next, I want to thank all my lab mates. Six years is a long time and I have seen many of my seniors moved on to become independent PI, do great science or next stage of their life. And I am always grateful for all the help I got from my seniors: Maulik is a good friend, and I am happy that he brought me in his project of probing NOS3 enzymatic activity. Aneesh is a good mentor and taught me a lot in the NOS2 project. Bhavya, Anand, Kasturi, Matt, Shareefa, Ved, Shabana were all great graduate students and achieved a lot in Krishnan lab. I also had the pleasure to work with postdocs including Kaho, Krishna, Nagarjun who all set good models. And even after they left the lab we will always be good friends. And I want to thank my junior graduate students, undergrads, new postdocs and technicians: Anees, Koushambi, Daphne, Joseph, Sourajit, Pravin, Sandip, Priyanka, Siddharth, JoAnn, Benton, Vanity. All of us really make a good team and I really enjoy doing research with the current members. Everyone is bringing in new techniques and really expand how we can approach exciting new projects with new biology.

Outside of labs I am also lucky to have people in my life who are always there when I needed. And I want to thank my friends and family for their unconditional support. My mother and father supported me to get bachelor's degree in the US and I appreciate how much my parents have

given up in order to support my education. Ph.D. was a tough journey, and my parents motivated me to push through and finish my degree. I would like to dedicate the thesis to all my extended family as well. My grandparents are all proud of whatever I have achieved. And I can never give back enough to my family for all their support over years.

In the last stretch of my Ph.D I met my fiancé Xia. I want to thank her for always being supportive and I am certain we will find happiness together. I would also like to thank God Almighty. He showed me the truth above all and continue to guide me to live and fight, all while enjoying His grace. He also put me in a group, His church, to help me grow and learn. It has been a great year to spend time together with my church group and I hope His will can prevail.

Junyi Zou

December 2022

List of Publications

(1) Jani, M. S.; **Zou, J**.; Veetil, A. T.; Krishnan, Y. A DNA-Based Fluorescent Probe Maps NOS3 Activity with Subcellular Spatial Resolution. *Nat. Chem. Biol.* **2020**, *16* (6), 660–666.

(2) Veetil, A. T.; **Zou, J**.; Henderson, K. W.; Jani, M. S.; Shaik, S. M.; Sisodia, S. S.; Hale, M. E.; Krishnan, Y. DNA-Based Fluorescent Probes of NOS2 Activity in Live Brains. *Proc. Natl. Acad. Sci. U. S. A.* **2020**, *117* (26), 14694–14702.

(3) Krishnan, Y.; **Zou, J.;** Jani, M. S. Quantitative Imaging of Biochemistry in Situ and at the Nanoscale. *ACS Cent. Sci.* **6**, 1938–1954 (2020).

(4) Zajac, M.; Anees, P.; Mukherjee, S.; Henn, K.; Oettinger, D.; Srikumar, J.; **Zou, J.;** Saminathan, A.; Krishnan, Y.; Molecular Identification of the Long-Sought Human Lysosomal Ca^{2+}/H^{+} Exchanger. *Submitted*

(5) **Zou, J.,** Mitra, K., Anees, P., Oettinger, D., Ramirez, J., Veetil, A. T., Krishnan, Y. Organellar sodium mapping reveals a role for lysosomes in salt adaptation. *Submitted*

Abstract

The mobilization and transport of Na^+ across the plasma membrane is central to biology[1,2]. While the sweeping consequences of aberrant extracellular or cytosolic Na^+ levels on organism physiology are known, and indeed mapped, at the tissue and single cell levels[3–5], sub-cellular Na^+ remains unmapped due to a lack of tools of sub-cellular imaging. Here we describe *RatiNa*, a pH-independent, ratiometric fluorescent reporter for Na^+. With *RatiNa* we successfully imaged organellar Na^+ in mammalian cells and *C. elegans*. Several crucial findings ensue from organelle Na^+ measurement: For one, average Na^+ levels in endocytic organelles exceeds cytosolic levels but can vary from one vesicle to another. In addition, unlike any other ion mapped so far, lumenal Na^+ decreases as endosomes mature. Finally, a drastic change in Na^+ levels occur in lysosomes when nematodes adapt to salinity. We found NHX-5, a putative lysosomal Na^+/H^+ exchanger, is vital for salt adaptation. Since lysosomes play a key role in metazoan metabolism, The ability to image sub-cellular Na^+ in vivo may lead to a deeper understanding of Na^+ transport and metabolism.

Introduction

i. Significance of organellar Na^+

Free sodium ion (Na^+) is the most abundant monovalent cation in most life forms[6]. The largest fraction is present in the extracellular milieu where it maintains the osmotic pressure and ionic balance. Na^+ is an essential nutrient: it cannot be produced endogenously and must be obtained from dietary intake[6,7]. We dedicate huge amount of energy and resources to preserve Na^+ in our body by kidney reabsorption as Na^+ is scarce in paleolithic diet[4]. However, there is an excess of Na^+ in our present day diets with cheap and easy access to processed food[8] (Figure 1). Our ability to evolve and thereby adapt to a high Na^+ modern diet is much slower, leading to excess dietary Na^+ being retained in our body, and disrupting the balance of ionic equilibrium[4]. Chronic excess dietary Na^+ is thus linked to several disorders such as hypertension, kidney failure and heart disease[9,10]. These diseases are on an alarming rise and ischemic heart disease is now the lead death cause of world population according to WHO[11]. Thus, a better understanding of Na^+ homeostasis could potentially identify ways to combating high Na^+ that causes pathology.

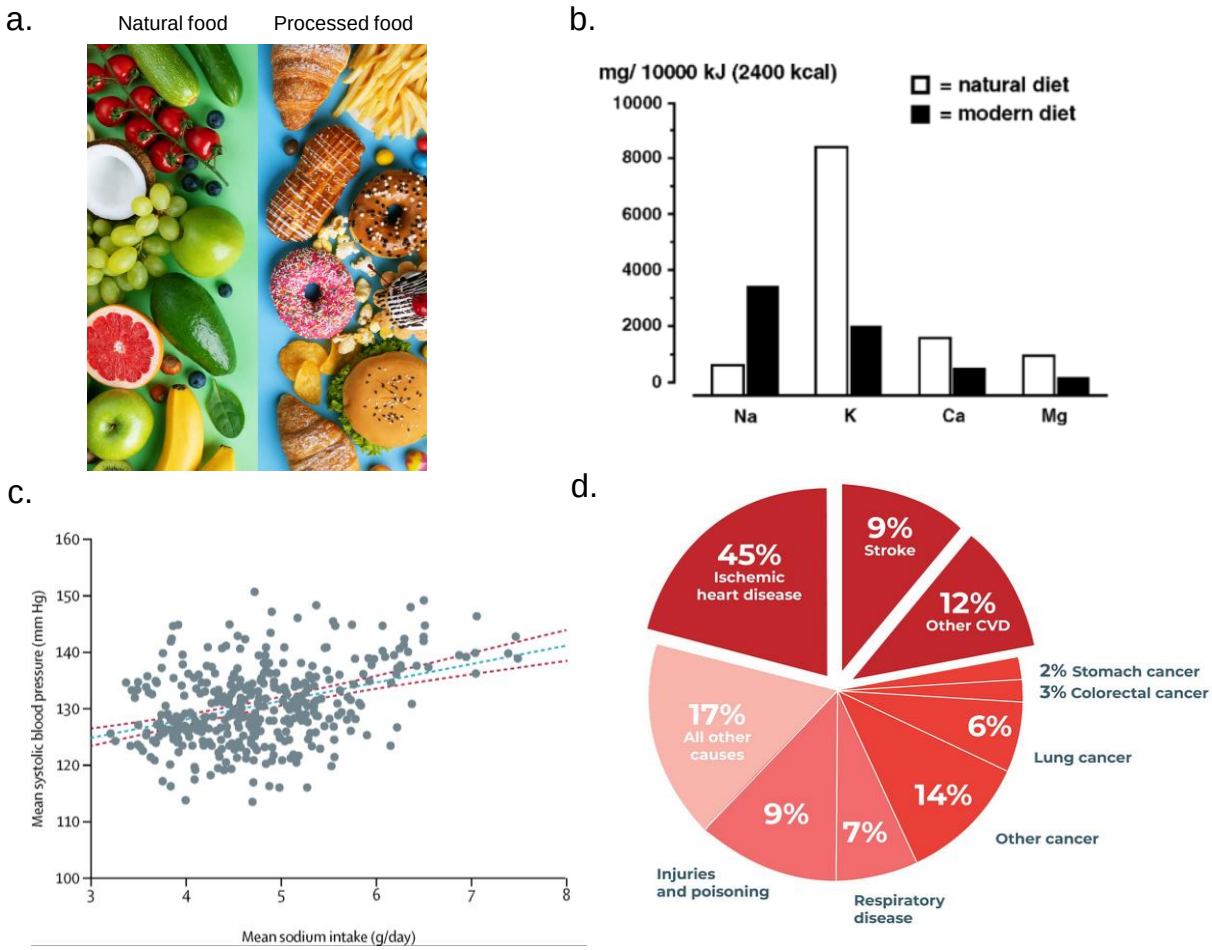

Figure 1. Na^+ is essential but in excess in modern diet

a. Examples of Natural food and processed food. b. Natural food has low level of Na^+ and processed food have high content of Na^+[12]. Graph is adapted from Karppanen et al. (reference 12). c. Large sample size study data showing clear correlation of Na^+ intake and elevated blood pressure. (N = 95,767 indivisuals)[13] Graph is adapted from Mente et al. (reference 13). d. Pie chart showing that cardiovascular disease is the leading cause of death in Europe, year 2017. Image source: https://www.r3i.org/.

Cells spend ~30% of their ATP to maintain the Na^+ gradient across the plasma membrane[14,15]. The Na^+ gradient regulates cell surface Na^+ channels and transporters that collectively maintain osmotic pressure and ionic balance as well as control functions ranging from neuron firing to nutrient transport[16,17]. Our current understanding of cellular Na^+ homeostasis is limited to its mobilization at the plasma membrane. Yet plasma membrane comprises only 2-5% of total membrane in the cell[18] and the remainder is distributed among organelles. The math alone suggests that Na+ homeostasis in the cell cannot be maintained just by the plasma membrane and organelles must be involved. Few lines of evidence suggest that organelles could contribute to the metabolism or mobilization Na^+ in single cells[19]. For one, organelles have quite different chemical environment compared to cytosol to perform their specific functions. Every ion that has been mapped so far in organelles shows levels that are quite different compared to either the cytosol or the extracellular milieu. Na^+ is one of the most abundant extracellular cations and is therefore also likely to vary given the differences in functions between different organelles. In addition, many organelles are now known to harbor membrane potential and organelle membranes contain several Na^+ channels and transporters[20–24]. For example, in yeast, many endosomal Na^+/H^+ exchangers (NHEs) were identified by salt stress causing lethality when these genes were knocked out[25]. I hypothesize therefore, that Na^+ gradient also exists across organelle membranes and that different organelles likely have different lumenal Na^+ levels.

The function and significance of maintaining Na^+ gradient across organelle membrane, if there is one, is unknown. One speculative reason is to maintain organelle membrane potential. Recently, organelles were found to have distinct membrane potentials ranging from +110 mV in lysosomes to +65 mV in recycling endosomes[20]. Such high membrane potential likely has a Na^+ transport component. As seen in the case of the plasma membrane, I posit that the Na^+ gradient across

organelle membranes can be used to depolarize the latter and trigger downstream events such as fusion and fission, Ca^{2+} release, etc.[26,27]. Another potential function for the organelle Na^+ gradient is to facilitate transport of other ions or amino acids through exchangers like NHEs[19] or transporters like SLC38A9, respectively[28]. Similar machineries have been found on the plasma membrane and is likely also present in organelles[29].

A key piece of evidence for the significance of Na^+ in organelles, is the fact that mutations in organellar Na^+ transporters lead to observable phenotypes such as a change in organism color. In the Japanese morning glory flower, mutation of vacuolar Na^+/H^+ exchanger nhx1 causes a change from purple to blue blossoms (Figure 2a) [30]. Even in animals, a mutation in zebrafish NCKX5, a K^+ dependent Na^+/Ca^{2+} exchanger in melanosomes, causes the typical zebrafish stripes to fade, and the lack of pigmentation, leads to the "golden" phenotype[31] (Figure 2b).

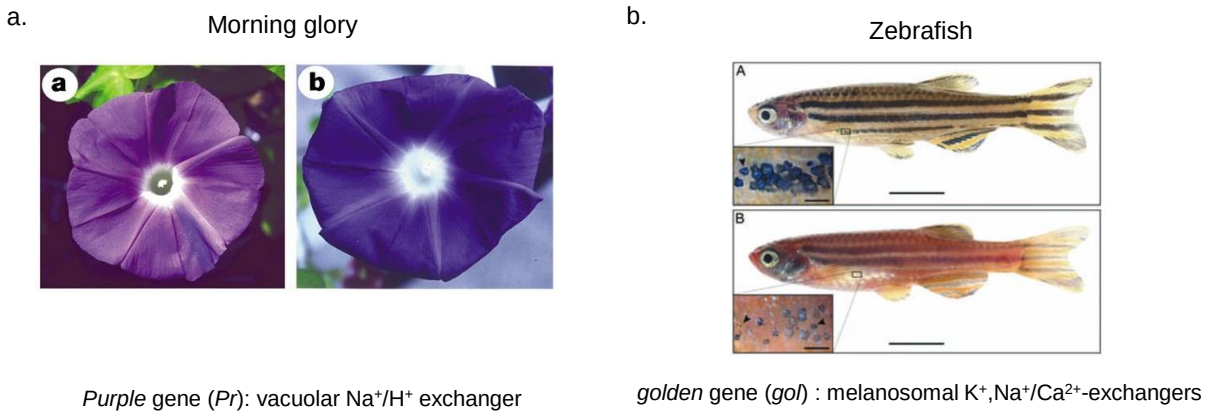

Figure 2. Organelle Na+ transporter dictates color phenotype. a. nhx1 gene mutation in morning glory causes flower to change from purple to blue color. Figure adapted from Fukada-Tanaka et al (ref. 30). b. nckx5 gene mutation in zebrafish cause the striping pattern to fade. Figure adapted from Lamason et al. (ref. 31).

ii. Developing a method to map Na^+ in organelles

To prove that Na^+ gradient exist at the organelle membrane we need feasible methods of Na^+ detection. Indirect methods like elemental analysis of isolated organelles reports only average values and cannot account for any ion exchange during the isolation process[32]. To answer questions about Na^+ function in organelles we used an imaging-based method which allows direct live imaging of Na^+ with single organelle resolution. Fluorescent probe development is a constantly evolving field and new technologies are emerging on a daily basis[33]. There are myriad ways to design fluorescent probes, but the working principle is simple: the fluorescent properties of the probe will change in the presence of different levels of the analyte that it is supposed to detect. One of the most popular scaffolds for fluorescent probes is based on proteins as they are genetically encodable[34]. For genetically encoded reporters, conformational change due to the binding of the analyte to the protein leads to a change in fluorescent intensity or FRET. Protein reporters can be easily expressed and targeted to a given organelle[35]. However, protein-based probes usually have low fluorescent intensity, limited dynamic range, limited responsivity compared to small molecules and its overexpression may change the physiological state of the cellular system[36]. There is no protein-based Na^+ reporter developed so far because there is no known Na^+ binding proteins (Figure 3b).

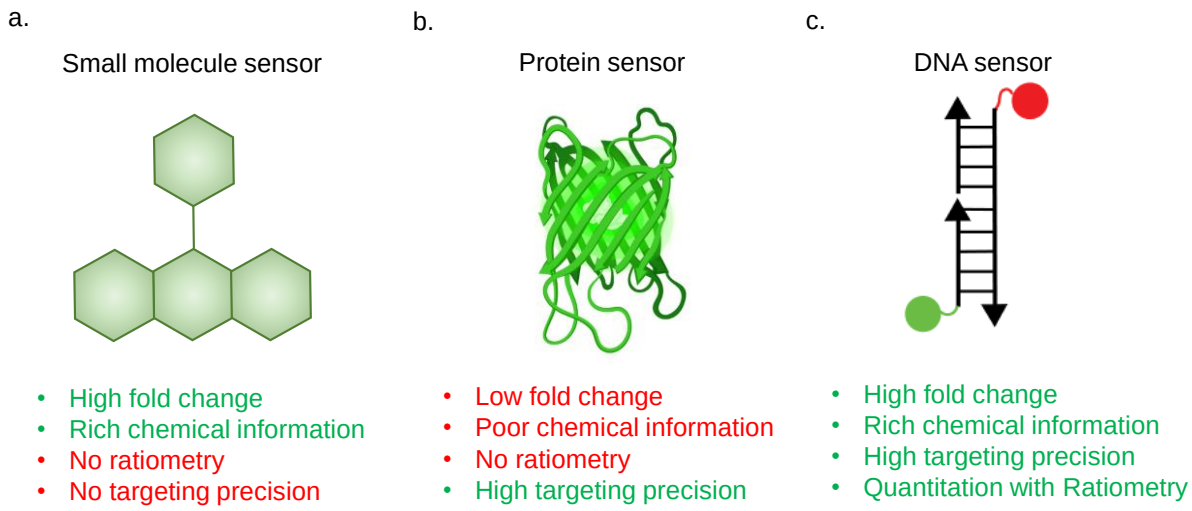

Figure 3. DNA based reporters combines the advantages of small molecule and genetically encodable reporters. Advantages and limitations of (A) small molecule fluorescent reporters and (B) protein based reporters. (C) DNA reporters have the advantage of small molecules for high fold change and richness of chemical information, as well as targeting precision associated with protein-based reporters. Internal ratiometry of DNA reporters allows accurate quantification.

On the other hand, small molecule probes have excellent photochemical properties and high fluorescence intensities[37] (Figure 3a). These fluorophores can either react to or associate with the analyte, resulting in fluorescence toggling on and off as a readout[38]. But organelle specific targeting is a major limitation of small molecule probes. Without any targeting motifs, such small molecule probes usually remain in the cytosol. But with functional groups appended on the small molecule, the probe can localize passively to certain organelles by leveraging the acidic pH of the organelle or its membrane potential[39]. But even same type of organelles can have different level of pH[40]: any ion transport on organelle membrane can lead to a substantial change in

concentration due to the small volume of organellar lumen[41]. Indeed, we have previously measured ion concentration and membrane potential in organelles and these parameters vary widely across a organelles[20,42,43]. Additionally, in disease states organelles usually have different chemical environments. For example, mitochondrial depolarization is accompanied by ROS induced stress[44]. Thus, many factors can affect targeting of small molecule probes to the correct organelles and a better strategy is needed to image organellar Na^+.

One way to improve the targeting specificity of small molecules is to use a biologics. DNA is an ideal candidate to target endocytic organelles (Figure 3c). Cells express scavenger receptors that bind and internalize to anionic macromolecules through clathrin mediated endocytosis[40]. Therefore, DNA can be delivered to endocytic organelles including endosomes and lysosomes by co-opting natural cellular machinery[45]. Unlike protein-based overexpression systems, DNA nanodevices cause no changes in cellular transcription/translation and can probe the resting state of live cells. One concern with treating cells with synthetic DNA nanodevices is their potential interaction with toll-like receptors (TLR)[46]. TLRs are expressed on innate immune cells surface that help immune cells identify threat of infection. dsDNA is a ligand for TLR9 and downstream signaling of TLR can change the cellular state and triggers unwanted immune response[47]. To address the concern, we have previously shown that short double stranded DNA of <100 bp, free of immunogenic sequences do not activate macrophages[48].

Using DNA as a scaffold to make organelle reporters has many more advantages. Duplex DNA is rigid upto 150 base pairs, and fluorophores can be positioned along this rigid rod at fixed distances to either prevent or enable photophysical interactions between different fluorophores[49]. Due to the 1:1 stoichiometry of Watson-Crick-Franklin base-pairing, one can incorporate reference fluorophores on a DNA assembly in a specific stoichiometry to make a uniwavelength

small molecule reporter, ratiometric. A fluorophore that is unaffected by target analyte creates a way to normalize fluorescent signal from a uniwavelength sensing dye. The ratiometric signal reports the concentration of analyte far more accurately as it is independent of reporter concentration[50].

Here I describe the development of a DNA-based ratiometric Na^+ reporter to measure lumenal Na^+ concentration of organelles which I name *RatiNa*. In the following chapters I describe *RatiNa* design, characterization, *in vitro* and *in vivo* performance. There are several key discoveries from my measurements of Na^+ with *RatiNa*. To begin with, my studies revealed the accurate levels of Na^+ in single lysosomes of both *C. elegans* and murine macrophage lysosomes for the first time ever. I found that Na^+ varied greatly across lysosomes and was on average ~40 mM. This indicates that when lysosomal Na^+ channels open, Na^+ must flow into the cytosol. Next, I mapped Na^+ as a function of endosomal maturation by measuring it in early endosomes, late endosomes and lysosomes. I found that, unlike any other ion mapped so far, lumenal Na^+ decreases along the endolysosomal pathway. To further shed light on the potential role of organelles in cellular Na^+ homeostasis, I mapped lumenal Na^+ levels in each stage of the endolysosomal pathway in worms upon their adaptation to high salt levels. I found that worms which successfully adapted showed substantial changes in their lysosomal Na^+ levels. In fact, worms lacking the lysosomal Na^+/H^+ exchanger NHX-5 failed to adapt. Using *RatiNa* I have pinpointed a key role for the lysosome in mobilizing Na^+ in the animal kingdom. *RatiNa* can reveal Na^+ metabolism at an entirely new level of cellular detail.

Chapter 1. Design and characterization of *RatiNa*

i. Existing Strategies for Na^+ measurement

The heart of the ability of *RatiNa* to sense Na^+ comes from a Na+ sensitive fluorophore. We started with a thorough search of small molecule Na^+ reporters in literature. Most existing Na^+ sensing molecules are based on Nobel Prize winner Charles Pedersen's finding of crown ethers, compounds that binds alkali metal ions[51]. SBFI is the first Na^+ sensing fluorophore developed by Roger Tsien in 1989[52] (Figure 4). The molecule consists of a crown ether for Na^+ binding and a benzofuran isophthalate fluorophore. The crown ether selectively binds to Na^+ and abolishes the photoinduced electron transfer (PET) quenching of the fluorophore from the lone pair of electrons on the crown nitrogen. It is self-ratiometric and has ~20 fold selectivity against K^+. However, it has 17 mM K_d for Na^+, a pKa of 6.09 and quantum efficiency of 0.045, indicating that it only senses Na^+ reliably up to 50 mM with low intensity and is sensitive to the acidic pH corresponding to organelle lumens. Subsequently, multiple new fluorophores with crown ethers were made and a few such molecules are worth mentioning. CoroNa Green is commercially available, has a relatively higher K_d of 80 mM and therefore is suited to measuring Na^+ in a higher concentration regime[53] (Figure 4, compound 4). ANa2 is a two photon active Na^+ sensing dye that can sense Na^+ in tissue[54] (Figure 4, compound 8). All existing Na^+ sensitive fluorophores are summarized in Figure 4.

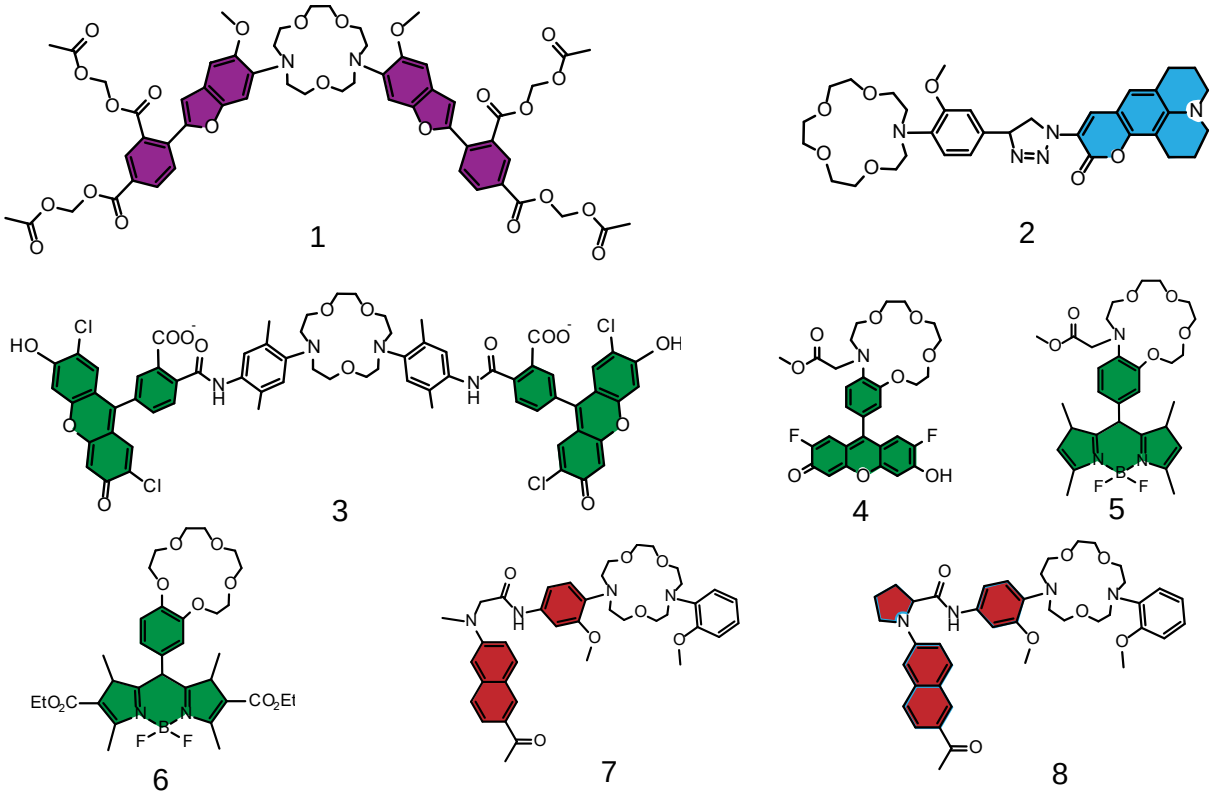

Figure 4. Published Na+ sensing small molecule probes. Chemical structures of published Na^+ sensitive fluorophores with their excitation wavelength shaded from UV (purple) to infrared (red).

Table 1. Spectral characteristics and dissociation constants for various Na^+ sensitive dyes.

Cpd no:	Dye name	Ex/Em Wavelength (nm)	K_d (mM)	Reference
1	SBFI	337/537	20	[52]
2	N/A	440/517	48	[55]
3	Sodium Green	507/530	8	[56]
4	CoroNa Green	492/515	80	[53]
5	N/A	498/510	59	[57]
6	N/A	497/507	N.D.	[58]
7	ANa1	780/500 (2 photon)	8	[54]
8	ANa2	750/500 (2 photon)	18	[59]

Strategies building on small molecule probes for Na^+ sensing are also developed. Verkman conjugated the Na^+ sensitive chromophore sodium red and Na^+ insensitive chromophore BODIPY-FL on polystyrene beads and estimated Na^+ in the colon pericryptal space of live mouse[60] (Figure 5a). On the other hand, reporters based on nucleic acids scaffolds are also known. Lu et al have isolated an RNA cleaving DNAzyme whose activity is highly dependent on Na^+[61]. They used it to make a Na^+ reporter by placing a quencher on the DNAzyme and a fluorophore on its substrate. Once Na^+ facilitates the cleavage of the RNA substrate, the fluorescence turns on[61,62](Figure 5b). Both strategies have limitations: beads cannot enter the cells, while the DNAzyme reports Na^+ via an irreversible reaction which cannot report Na^+ fluctuations.

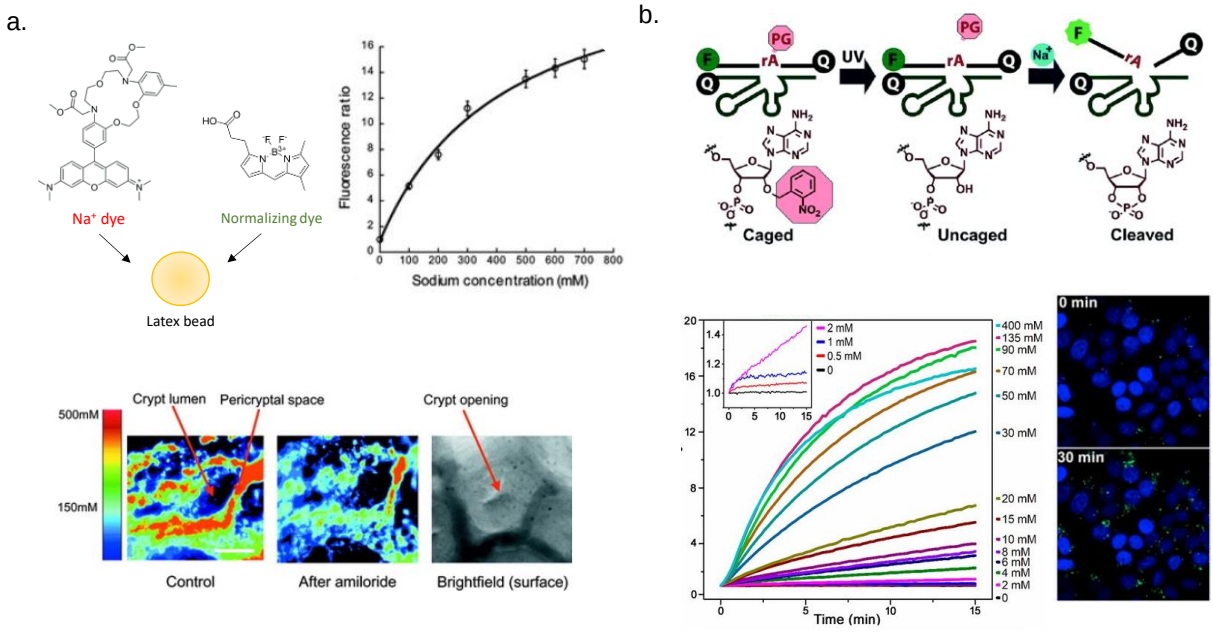

Figure 5. Non-small molecule Na+ probing strategies a. Ratiometric bead-based Na^+ sensing by Verkman et al. Using Na^+ sensing dye Sodium Red and ratiometric dye BODIPY-fl non-specifically adsorbed to latex beads, the authors measured Na^+ in the pericryptal space of mice

(Figure 5 Continued) colon. Figure is adapted from Lu et al. (ref. 51). b. DNAzyme based bioreporter. Single RNA cleavage site is photocaged and the reporter is delivered to cells. After uncaging, the DNAzyme cleaves the RNA and quenching is relieved. Figure is adapted from Verkman et al. (ref. 53).

ii. Design of *RatiNa*

All summarized strategies have distinct advantages and disadvantages and there is no universal method to detect Na^+ in all biological and cellular locations. The biggest obstacle for organelle Na^+ sensing is the acidic lumenal environment in endocytic organelles which crossreacts with every known Na^+ sensitive dye[63]. We were inspired by a recent paper demonstrated that the hydroxyl group of Aarhus Green (Figure 6a, 6b), a tetrafluorofluorescein fluorophore, exhibits lower pKa (~3.1) and less pH sensitivity from pH 4 – 7 as compared to Pennsylvania Green (Figure 6B), its difluorofluorescein analogue (pKa ~ 4.7)[64]. CoroNa Green (Figure 6c) is also a difluorofluorescein Na^+ sensing molecule that we can potentially apply the same strategy to engineer to shift the pKa to lower regime to obtain a pH insensitive yet Na^+ sensitive small molecule that we named Chicago Green (CG) (Figure 6c). It has a tetrafluorofluorescein core, a crown ether and a propargyl group for conjugation to DNA scaffold. The detailed synthesis of

CG is described in next section.

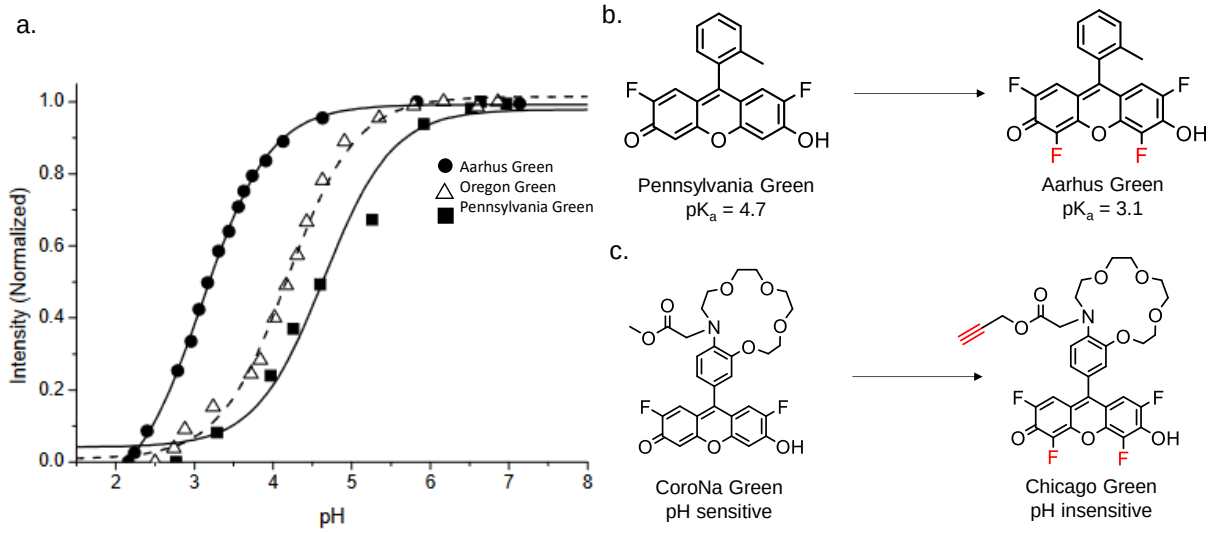

Figure 6. Rationale for chemical design of Chicago Green. a. pH response of fluorescence of Aarhus Green and Pennsylvania Green. Figure adapted from Holmehave et al. (ref. 64). b. Structure and pKa of Aarhus Green and Pennsylvania Green shows the additional fluorine modification shifts pKa and makes the fluorophore less sensitive to pH. c. Chicago Green is designed by fluorine modification of CoroNa Green, an Na^+ sensing dye with physiological K_d and high fold change to Na^+.

I designed the DNA scaffold shown in Figure 7. A 45-bp duplex was chosen as the DNA backbone. The length of the duplex is ~15 nm and the two fluorophores are placed at opposite ends of the DNA duplex to make sure no interference or FRET can happen between the dyes. In a separate study my colleague Dr Anees Palapuravan has found that DNA sequences next to a cryptand, another crown ether, based fluorophore can affect the dye performance. Therefore, the sequence which had no effect on cryptand dye was chosen for CG conjugation. The final design for *RatiNa* consists of three single stranded DNA: D1 is a 25-mer ssDNA with CG at 5' end. The

normalizing module D2, bearing ATTO647N (λ_{ex}= 646 nm, λ_{em} = 663 nm) at the 5' end, is a 45-mer ssDNA with a sequence complementary to D1. Our choice of ATTO647N as the ratiometric dye is based on its brightness, photostability, insignificant spectral overlap with CG and insensitivity to pH, Na+ and other ions[65]. D3 is a 20-mer ssDNA that can be either unmodified or with a biotin conjugated for bead clamping later described.

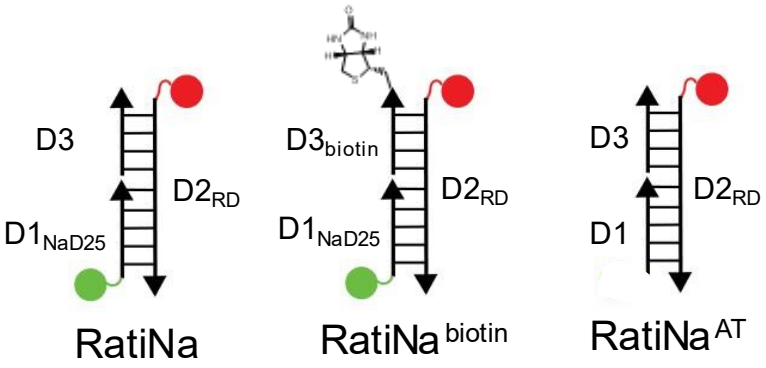

name	sequence
$D1_{NaD25}$	5'-CG-ATC AAC ACT GCA TAT ATA TAC GAC C-3' (25mer)
D1	5'-ATC AAC ACT GCA TAT ATA TAC GAC C-3' (25mer)
$D2_{RDL}$	5'-ATTO647N-C ACT GCA CAC CAG ACA GCA A G GTC GTA TAT ATA TGC AGT GTT GAT-3' (45mer)
$D3_{biotin}$	5'-T TGC TGT CTG GTG TGC AGT G-BioTEG- 3' (20mer)
D3	5'-T TGC TGT CTG GTG TGC AGT G – 3' (20mer)

Figure 7. Design and sequences of of DNA based RatiNa reporters. *RatiNa* comprises three single stranded DNA oligonucleotides with two fluorophores. CG (green sphere) is the Na^+ sensing fluorophore and ATTO (red sphere) is the ratiometric fluorophore. *RatiNa*^{biotin} can be displayed on streptavidin coated beads for calibration with microscope. *RatiNa*^{AT} is used for colocalization experiments and bears only the ATTO dye.

iii. Synthesis of Chicago Green, a pH insensitive Na^+ sensing dye

We followed previous literature for synthesis of compound 3-5[66]. The synthesis of CG was performed by Dr Koushambi Mitra, Dr Aneesh Tazhe Veetil and Joseph Ramirez and following protocol is adapted from Dr Mitra's note (Figure 8). In brief, a mixture of 2-aminophenol (1 eq) and cesium fluoride (5 eq) was stirred in acetonitrile in N_2. Next, tetraethylene glycol di(p-toluenesulfonate) (1 eq) was dissolved in acetonitrile and added to the mixture and let react for 48 h in N_2. Crude product was collected by evaporation and dissolved in chloroform and washed with water, saturated sodium bicarbonate and brine. Silica gel column chromatography (50-70% ethyl acetate/hexane) was used for purification and final product is a yellowish-brown oil. Next, compound 3 (1 eq), methyl bromoacetate (2 eq), DIPEA (5 eq) and NaI (1 eq) mixture in dry acetonitrile was refluxed in N_2 for 48 hours. Crude product was evaporated and dissolved in dichloromethane and washed with water. Organic layer was dried with $MgSO_4$ and evaporated. Silica gel column chromatography (0-8% methanol/dichloromethane) was used to purify compound 4. $POCl_3$ (5 eq) was slowly added to dry DMF to form the Vilsmeier's reagent. Compound 4 (1 eq) was slowly added to Vilsmeier's reagent, and the reaction was stirred for 24 h at room temperature in N_2. Reaction mixture was slowly poured into a mixture of ice-cold saturated K_2CO_3 solution. After 5 times extraction of dichloromethane, the organic extract was dried with Na_2SO_4 and purified with silica gel column chromatography (0-8% methanol/dichloromethane) to yield compound 5. Compound 5 (1 eq) and NaOH (3 eq) were dissolved in 1:1 EtOH/H_2O and stirred at room temperature for 2.5 h. Then 3 N HCl was used to neutralize the solution and EtOH was evaporated. 5 times extraction of dichloromethane was used and the extract was washed with brine and dried with Na_2SO_4. After evaporation, propargyl

alcohol (1.2 eq), DIPEA (1.2 eq) and DMAP (0.2 eq) was added to crude product in dichloromethane in ice bath. EDC (1.2 eq) was added to the mixture and reaction was stirred at room temperature for 16 h. The reaction was then double washed with water and brine, dried with Na_2SO_4, and evaporated. Silica column chromatography (0-5% methanol/dichloromethane) was used to for purification of compound 6, a yellow viscous oil. Compound 6 (1 eq), 2,4-difluororesorcinol (2 eq) was then stirred in methanesulfonic acid at room temperature for 48 h in N_2. The reaction mixture was diluted with water and slowly poured into ice-cold 3 N NaOAc solution and extracted with ethyl acetate for 5 times. Organic extract was dried with Na_2SO_4, filtered and evaporated. Crude product was mixed with chloranil in 1:1 chloroform/methanol and refluxed for 4-5 h. Reaction mixture was cooled, filtered and evaporated. Reverse phase HPLC (1:1 methanol/acetonitrile) was used to obtain final product propargyl-CG. Mass spectrometry and NMR confirmed the identity of all intermediates and products.

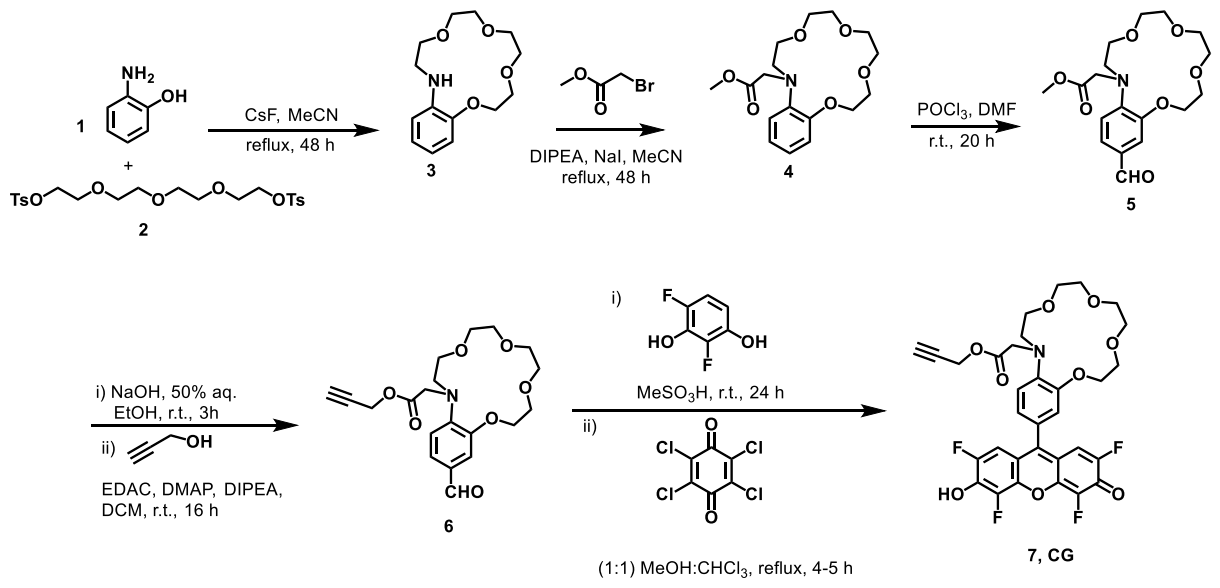

Figure 8. Synthesis of Chicago Green. A brief overview of the synthesis schematic for the synthesis of Chicago Green. Synthesis schematic is adapted from Dr. Koushambi Mitra.

CG was then characterized by spectroscopy. We found the excitation maximum and emission maximum of CG to be 510 nm and 530 nm respectively (Figure 9a). CG is indeed responsive to Na^+ with a 6.5 fold change from 1 mM to 150 mM of Na^+ in buffer (Figure 9b, 9c). Most importantly, we observe similar K_d from pH 4.5 – 7.4 indicating CG is indeed pH insensitive (Figure 9d). Previously we have noticed that small molecule reporters can have altered fold change or spectral characteristics after DNA conjugation[48]. Therefore, we proceeded to conjugate CG to DNA and performed a thorough characterization with the full reporter.

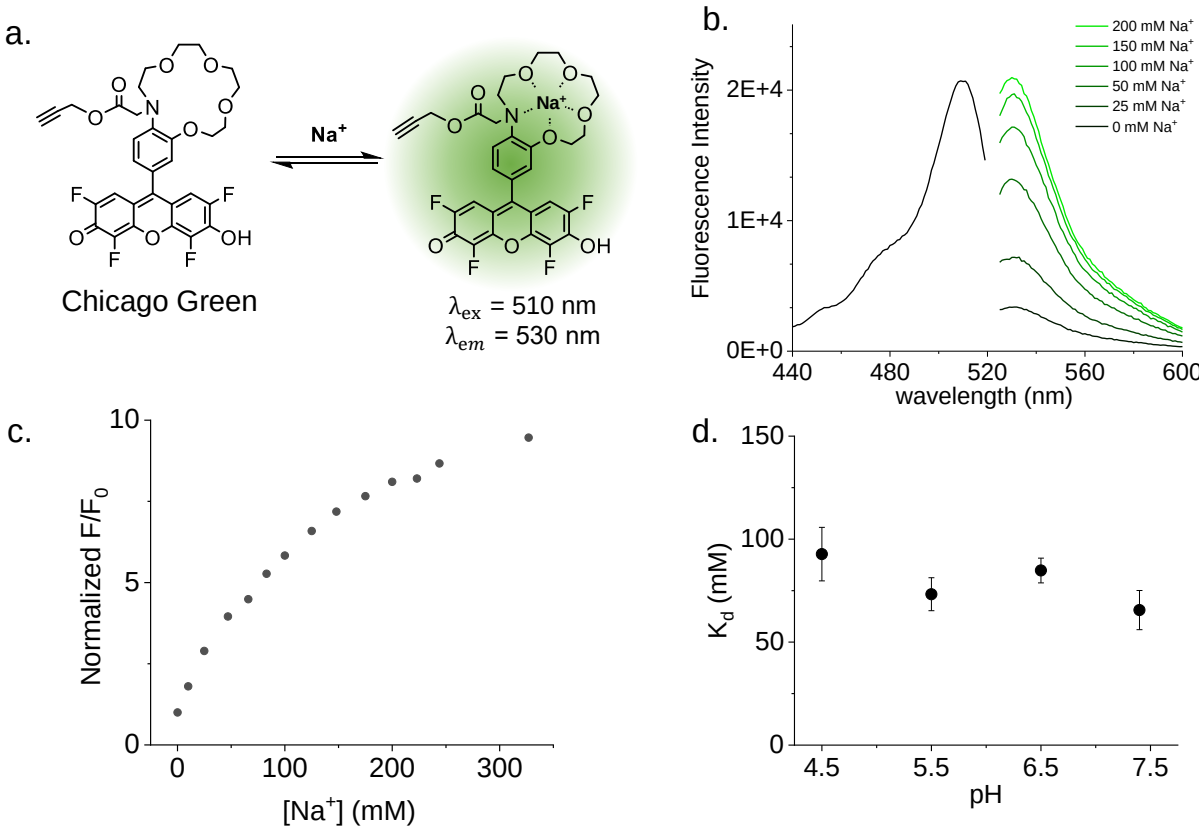

Figure 9. Chicago Green is sensitive to Na+ and insensitive to pH. a. Structure and mechanism of Na^+ mediated fluorescence increase of CG. b. Excitation and emission spectra of

(Figure 9 Continued) CG. Emission fluorescence increases with increasing amounts of Na^+. c. CG Emission peak maximum plotted against Na^+ level at pH 7.4. d. K_d of CG is calculated from Na^+ response curve at each pH point.

iv. CG conjugation to DNA

Next, I will describe how to build *RatiNa* reporters. As discussed previously the reporter is composed of three single stranded DNA. Two of the strand D2 and D3 are directly purchased from vendor. We will need to perform CG conjugation to D1 strand and anneal with the other two strands for complete *RatiNa* reporters (Figure 10a). We started by using D1 strand with 5' amine modification. 5'-amine modified single strand DNA (IDT) is reacted overnight with 20 equivalence of azide-(PEG)4-NHS ester (Click Chemistry Tool, AZ103) in 100 mM Na_2HPO_4 buffer with pH adjusted to ~8.5 by adding $NaHCO_3$. Ethanol precipitation of DNA was done by adding 0.1 volume of 3 M NaOAc (Sigma) and 3 volume of molecular biology grade ethanol (Sigma). Precipitation was done at -20 °C for at least 2 hours then centrifuged at >12000 g to collect DNA precipitate. DNA was redissolved in 50 mM pH 7 phosphate buffer after wash with 70% ethanol (Figure 10b).

To confirm full conversion of amine to azide, a small aliquot of azide-DNA was reacted with 2 equivalences of 5kDa mPEG-DBCO (Nanocs, PG1-DB-5K) in 50 mM pH 7 phosphate buffer overnight and run on 12% native PAGE. PEGylated DNA will have significantly different gel shift and no azide-DNA band is observed, indicating all amine strands are converted to azide strands (Figure 10c). Azide-DNA can be made in bulk and aliquoted in -20 °C for 12 months.

The copper(I)-catalyzed alkyne-azide cycloaddition (CuAAC) reaction was used for CG conjugation to azide-DNA[67] (Figure 10d). Copper catalyst was prepared by premixing concentrated $CuSO_4$ and THPTA (100 mM, 10 eq). Purge azide-DNA (1.3 mM, 1 eq) with nitrogen for 1 min. Add propargyl-CG (2.6 mM in DMSO, 2 eq) CuSO4/THPTA mix, and sodium ascorbate (1 M, 40 eq) in 30% DMSO in buffer. Extra DMSO may be needed to fully dissolve small molecule propargyl-CG. Reaction mix was briefly purged with nitrogen and tube was sealed and allow to react for > 5 hours. DNA was precipitated and assessed by both 12% native PAGE and UV-Vis. D1 band in PAGE shows CG fluorescence confirming that reaction has occurred. Absorption spectrum of CG-D1 conjugate confirmed full conjugation of DNA strands by extinction coefficient analysis (ϵ = 21,000 L / mole·cm for CG at 522 nm). We noticed that λ_{ex} and λ_{em} are shifted to 522 nm and 545 nm respectively, a change potentially occurred due to structural changes on CG from propargyl group to triazole group after conjugation to DNA. The fluorescence fold change of CG to Na^+ is preserved after conjugation to DNA.

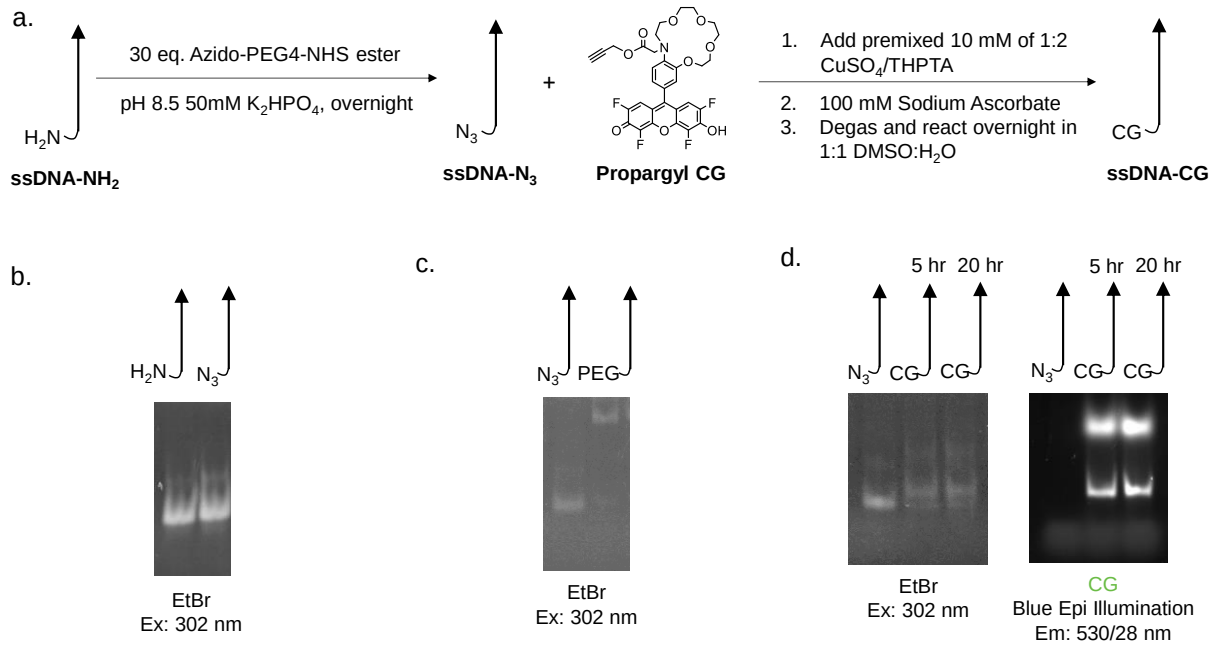

Figure 10. CG conjugation to DNA verified by PAGE. a. Reaction schematic of CuAAC coupling of CG to ssDNA. b. PAGE analysis of first conjugation step, azido strand shows no gel shift from amine strand. c. PAGE confirmation first conjugation step by reacting azido strand with 10kDa PEG. The full conversion of azido strand to PEGylated strand confirms that no amine strand is present. d. PAGE of CG to DNA conjugation. CG fluorescence can be detected from the DNA band.

Next complete *RatiNa* reporters are formed by annealing (Figure 11a). We made *RatiNa* which has unmodified D3 strand and *RatiNa*^{biotin} to replace D3 with biotinylated 3' end. 12% PAGE gel shows the complete annealing of *RatiNa* reporters with no extra single stranded DNA band to guarantee 1:1 ratiometry (Figure 11b). And the complete *RatiNa* has both red fluorescence from

ATTO647N and green fluorescence from CG.

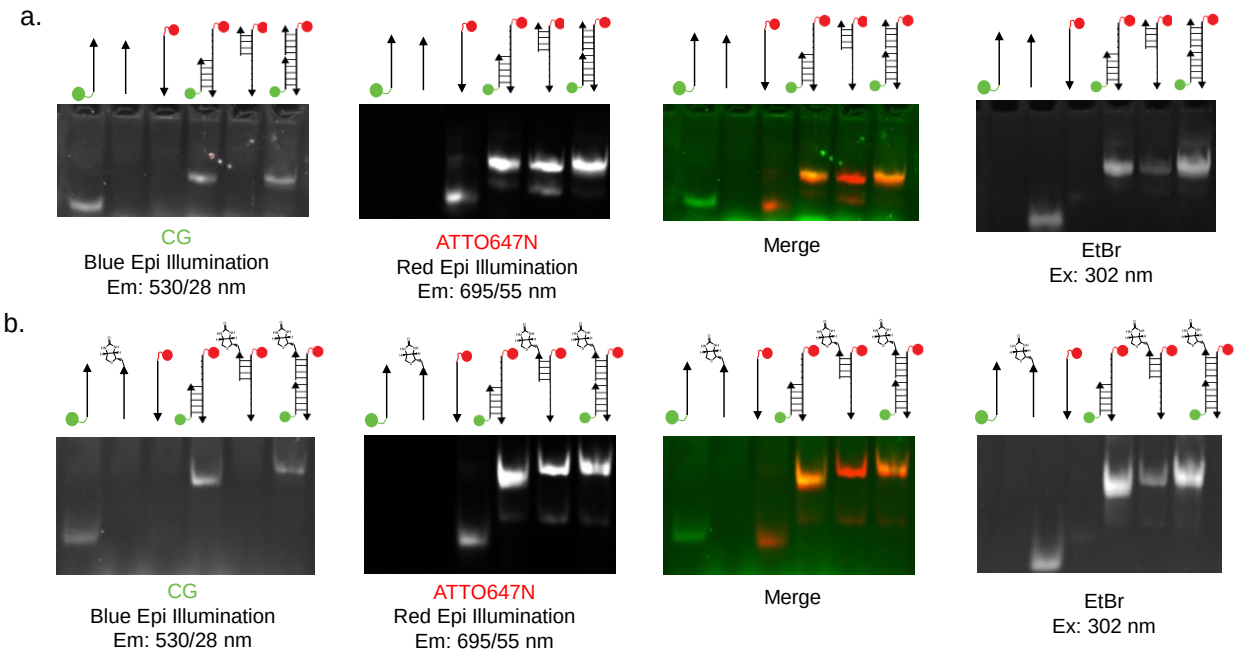

Figure 11. RatiNa reporters annealing confirmed by PAGE. a. 12% native PAGE shows full annealing of *RatiNa* reporter with no single strands or partially annealed products. b. 12% native PAGE shows full annealing of *RatiNa*^{biotin} reporter with no single strands or partially annealed products. Arrow represents ssDNA, green circle represents CG dye and red circle represents ATTO dye.

v. *RatiNa* is selective to Na^+ and pH insensitive

We first take fluorescence spectra of *RatiNa* for Na^+ sensitivity in Na^+ buffer (150 mM Na^+ and K^+, 150 mM Cl^-, 10 mM HEPES, 10 mM MES, 10 mM KOAc. pH adjusted by HCl or KOH). The buffer mimicks Na^+ and K^+ level in biological system: total amount of both cation is about 150 mM. HEPES, MES and KOAc combined can buffer pH from 3-9.

To fully characterize *RatiNa* in terms of Na^+ affinity, pH insensitivity and selectivity, we decided to use fluorescent imaging method since the fluorescence signal is the final read out. Thus, we can image *RatiNa* with same image acquisition settings as we use for both in vitro characterization and in vivo measurement. To image *RatiNa* we use the biotinylated *RatiNa* to coat streptavidin bead with *RatiNa* and image the bead in various buffer conditions. In brief, 1 μm streptavidin coated polystyrene bead (Bangs Laboratories, CP01004) was first washed twice and then incubated with 10 μM of $RatiNa^{biotin}$ in phosphate buffer. Either vigorous shaking or magnetic stirrers can be used to keep beads well mixed. After 2 hours of shaking the bead can be collected by centrifuging at 5,000 rpm and stored in phosphate buffer. 0.1% Tween-20 was added to prevent aggregation of beads.

Beads were then imaged to test Na^+ affinity. *RatiNa* beads were resuspended in Na+ buffer (1 mM to 2000mM NaCl, 10 mM HEPES, 10 mM MES, 10 mM KOAc. pH from 4.5 to 7.4 adjusted by HCl or KOH) and added to poly-D-lysine coated glass bottom dishes (Cellvis D35-14). Poly-D-lysine coating help with immobilization of the beads. Bead was imaged by either wide field microscope (Olympus IX83) or confocal microscope (Leica Stellaris 8). Individual bead was first picked with Analyze Particle function in FIJI and saved as individual ROI. Then each ROI was analyzed by taking integrated intensity in CG channels and ATTO channels. Average G/R for >100 beads were calculated and normalized to the lowest average G/R in all samples (Figure 12a). We notice that on the log scale normalized G/R can be approximated with a sigmoidal curve (Figure 12d). This is expected response for affinity-based fluorescent reporter.

For pH insensitivity we compared the sigmoidal curve at each pH from 4.5 to 7.4. From the overlay and Kd calculations, we concluded that both fold change and Kd are constant from acidic to neutral pH (Figure 12c). Since the lysosome is most acidic organelle with average pH of 4.5[63].

RatiNa can reliably measure Na+ in acidic organelles, and we expect to see the same Na+ response regardless of pH.

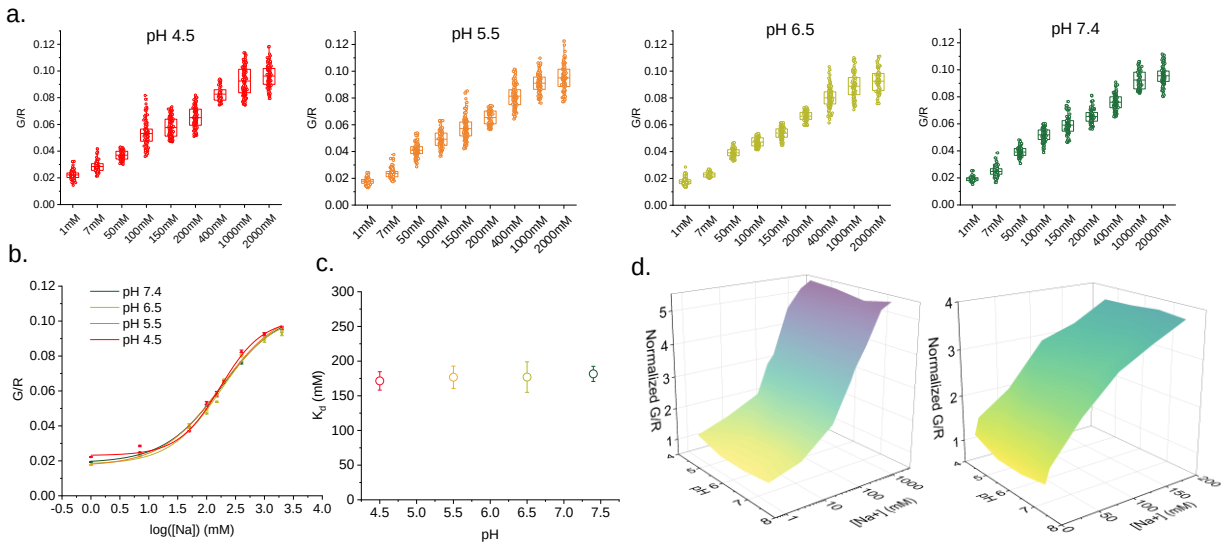

Figure 12. Bead calibration of RatiNa for Na+ and pH response. a. *RatiNa* bead was imaged in pH = 4.5, 5.5, 6.5 and 7.4 Na^+ calibration buffer and imaged with widefield microscope. G/R of more than 100 beads was calculated. G/R signal increases and saturated at high Na^+. b. G/R and log([Na^+]) is plotted and sigmoidal fit shown for each pH. The fitted curves from pH 4.5 to 7.4 shows that *RatiNa* is pH insensitive. c. Na^+ K_d of *RatiNa* calculated from the sigmoidal fit. K_d values are also constant from pH 4.5 to 7.4. d. Surface plot of *RatiNa* G/R signal across different pH and Na^+ level. *RatiNa* G/R response plotted in physiological Na^+ level in linear scale. In this Na^+ range G/R increase is approximately linear with >3 fold change.

Selectivity of *RatiNa* is another crucial aspect for biological application. It is widely recognized that crown ether can bind to Cs with superior affinity[68] but we limit our test to biologically abundant ions: K^+, Li^+, Mg^{2+}, Ca^{2+}. These ions were added at biologically relevant concentration

(145 mM KCl / 10 mM LiCl / 10 mM $CaCl_2$ / 10 mM $MgCl_2$) to *RatiNa* in background of 5 mM Na^+ (Figure 13a). *RatiNa* beads were imaged, and signal was compared before and after addition of ions. We found that the increase of signal was insignificant. To test whether general osmolarity increase can affect *RatiNa* signal, we also added 300 mM NMDG, an organic monovalent cation. No signal increase was observed, and we concluded that in biological environment, *RatiNa* is only responding to Na^+ and not any other major cations. Since K^+ is the main cation that can affect Na^+ signal of *RatiNa*, We also measured *RatiNa* signal increase with K^+ (Figure 13b). We found that only in molar range of K^+ we see ~1.2 fold increase of *RatiNa* signal, and the selectivity against K^+ is 27 fold.

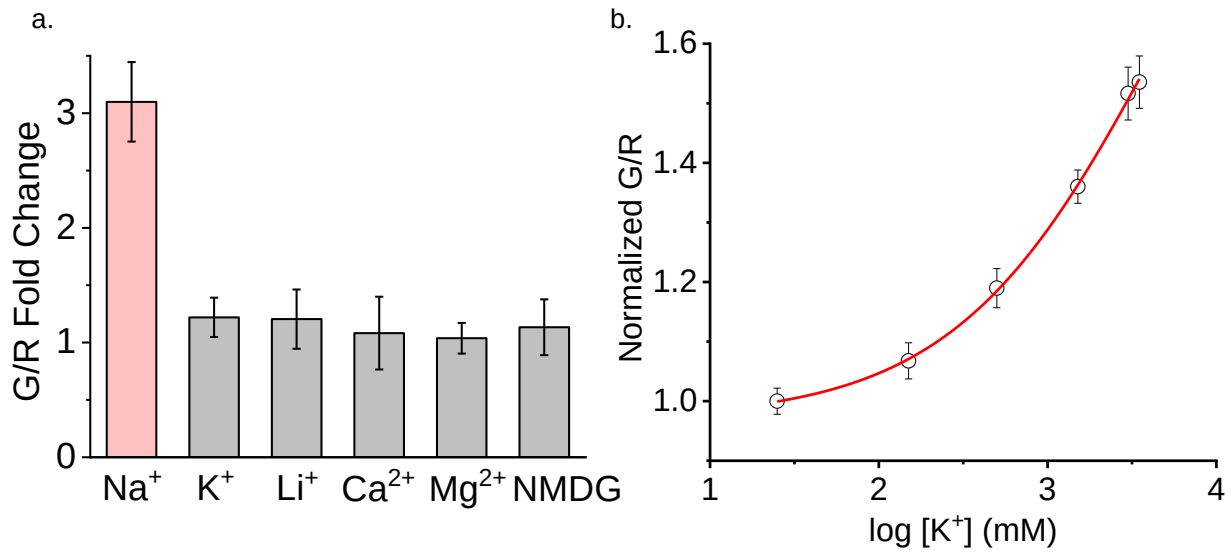

Figure 13. Selectivity of RatiNa and its K+ binding characteristics. a. Specificity of *RatiNa* reporter against other physiologically relevant cations. Na^+, K^+ = 145 mM; Li^+, Ca^{2+}, Mg^{2+}, NMDG = 10 mM. b. *RatiNa* signal increase with high amounts of K^+. K_d for K^+ is 4500 mM and selectivity against K^+ is ~27 fold.

Chapter 2. Calibration of *RatiNa* and In vivo measurement

i. Requirements of calibration due to low fluorescence of CG

Having fully characterized *RatiNa* in vitro by fluorescence spectroscopy and microscopy, here I describe how we used *RatiNa* to measure Na^+ in organelles of living systems. We chose to test *RatiNa* in *C. elegans* and macrophages for several reasons. Firstly, in both systems we have previously established targeting to endocytic organelles[48,69]. Secondly, *C. elegans* coelomocytes and macrophages uptake significant amount of DNA due to high expression of scavenger recepters[70,71]. Finally, we have previously measured the concentration of H^+, Cl^-, Ca^{2+} and membrane potential in both *C. elegans* and macrophages but organellar Na^+ is yet to be measured in either system. Organelle Na^+ measurement would complement our knowledge of other ions measured and help us understand the overall landscape of the chemical milieu within organelles.

One of the biggest obstacles I faced in using *RatiNa* in live cells was low fluorescence signal and suboptimal signal to noise ratio for reliable ion measurement in organelles. CG has remarkable selectivity and pH insensitivity. However, like all other Na^+ sensing small molecules, it is limited by the brightness of the dye. We have measured the relative quantum yield by comparing to Rhodamine 6G, a dye with similar absorption spectrum ($\lambda_{max} = 535\ nm$) and known quantum yield ($\phi = 0.95$ in H_2O). We found that CG has a quantum yield of 0.045 when fully turned on using the following equation to compare relative quantum yield[72] (Figure 14a, 14b):

$$\phi_{CG} = \phi_{Rhod}\left(\frac{Grad_{CG}}{Grad_{Rhod}}\right)\left(\frac{n_{CG}}{n_{Rhod}}\right)^2 = 0.045 \qquad \text{Eq. (1)}$$

$Grad_{CG}$ and $Grad_{Rhod}$ refers to the gradient of the linear fitting curve of absorbance maximum plotted against fluorescence maximum of two fluorophores. n_{CG} and n_{Rhod} refers to the refractive

index of the sample and cancels out because both measurements are done in pure H_2O. compared to a quantum yield of 0.65 for ATTO647N[65] and therefore CG has overall low brightness.

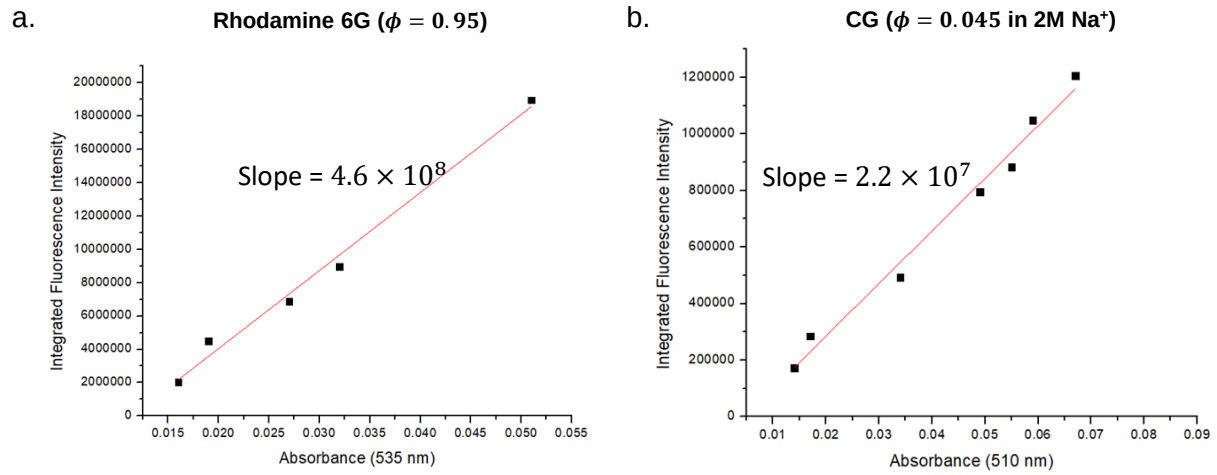

Figure 14. Relative quantum yield of CG. Rhodamine 6G with known absorbance and fluorescence spectroscopy (A) of exciting at 535 nm and emission at 550 nm. Absorbance of CG sample are recorded (B), and fluorescence were taken at 550 nm. Slopes of linear fitting curve of both graphs are calculated to determine the relative quantum yield of CG.

On beads, since there is no background fluorescence, *RatiNa* has homogeneous signal due to high effective concentration from strong interaction of streptavidin and biotin. However, the *RatiNa* signal from an organelle can be masked by autofluorescence within the cell, especially if there is a low level of uptake of DNA nanodevices in a given system. Therefore, to get reliable measurement we must calibrate *RatiNa* in the same system where we intend to measure Na^+.

One way to get the best fluorescence signal out of a low intensity dye like CG is to excite and collect emission at optimal wavelength. The excitation peak wavelength for CG conjugated to DNA is 522 nm which is between traditional 490 nm GFP and 550 nm RFP channels. We use

525/30 BP (Semrock FF01-525/30-25) as excitation filter, 532 nm dichroic mirror (Semrock Di02-R532-25x36) and 575/40 BP (Chroma ET575/40m) as emission filter on the wide field microscope for the CG channel. *RatiNa* beads in these channels gives good fold change and signal to noise ratio. However, in cultured cells CG channel is much harder to visualize compared to images of beads. Firstly, lysosomes in cultured cells have less *RatiNa* compared to individual beads. Secondly, the autofluorescence signal is high and can mask the *RatiNa* CG signal. Thirdly, the autofluorescence signal is heterogeneous and cannot be simply excluded from background analysis or image processing.

Given that the difficulty to image CG arises mainly from the background, we use confocal microscopy to reject "out-of-focus" light in effort to improve the signal to noise. We chose Leica Stellaris 8 confocal microscope which has a white light laser and can excite a fluorophore of any wavelength from 440 nm to 790 nm. We found that when set excitation at 522 nm and detector to collect from 530 – 580 nm, signal to noise of CG channel is much greater than widefield microscope in cultured cells. Therefore, we decided to do bead clamping, cell clamping and measurements in this confocal microscope.

ii. Targeting endocytic organelles of *C. elegans*

C. elegans is an established model system to validate DNA based reporters[43,73,74] as it presents many advantages. For one *C. elegans* has 6 cells called coelomocytes which are dedicated for removing and degrading unwanted materials. Coelomocytes express high level of scavenger receptors, which are natural receptors that mediate the endocytosis of double-stranded DNA, . We have observed that coelomocytes uptake essentially all dsDNA that is injected into the pseudocoelom of the worm and cell specificity is cleanly achieved. Coelomocytes also have big endosomes and lysosomes, and are actively endocytosing cells. This helps to accumulate large

amounts of DNA reporters leading to excellent signal to noise ratio and this eventually helps with image analysis. Secondly, knockdown and knockout of *C. elegans* genes can be easily done and existing library of mutant strains are readily available. Thirdly, *C. elegans* is small, transparent and has no pigments that might interfere with live fluorescent imaging.

DNA nanodevices are directly microinjected to the pseudocoelom of the worm body, which targets the endocytic compartments of coelomocytes. Before doing measurements we try to standardize targeting of specific organelles of *C. elegans*. We made *RatiNa*^{AT} which share the same D2 and D3 with regular *RatiNa* but D1 is not conjugated to CG dye. *RatiNa*^{AT} can be used for verifying targeting because it has identical DNA backbone which is therefore trafficked the same as regular *RatiNa*. And only ATTO dye is needed to visualize the location of DNA.

Young adult worms were injected with 2 μM *RatiNa* in the pseudocoelom following previously published work[74] and transferred to fresh NGM plates. Worms were then transferred to agar pads (2% agar in M9 buffer). 50 μM levamisole was used to anesthetize worms. Worms were imaged at the indicated chase times.

RatiNa targets organelles through scavenger receptor mediated endocytosis. Endocytosed cargo traffics through organelles on the endolysosomal pathway in a time dependent manner. Cargo is trafficked first to early endosomes, then to late endosomes and finally reaches the lysosome. If we image at specific chase times, *RatiNa* is found to be localized mostly in the early endosome, late endosome or lysosomes. We have previously established these timepoints in *C. elegans* with other DNA based reporters. Now we need to determine the effectiveness and specificity of *RatiNa* targeting using these timepoints.

For early endosome targeting we used *cdIs131* worm which expresses GFP::RAB-5 fusion protein in coelomocytes. RAB-5 is an early endosome protein marker[75]. Worms were imaged 5 min after injecting *cdIs131* worm with *RatiNa*^{AT} (Figure 15a). *RatiNa*^{AT} colocalizes with early endosomes 5 min after injecting *cdIs131* worms For late endosome targeting we used *cdIs66* mutant worms which express GFP::RAB-7 fusion protein in coelomocytes. RAB-7 is a late endosome protein marker[75]. *RatiNa*^{AT} colocalizes with late endosomes 17 min after injecting *cdls66* worms . For lysosome targeting we used *pwIs50* mutant worms which express GFP with LMP-1 promoter. LMP-1 is a lysosomal protein marker[76]. *RatiNa*^{AT} colocalizes with lysosomes 60 min after *pwls50* worms are injected.

Colocalization analysis is used to confirm targeting to specific organelle. In *C. elegans*, endosome and lysosome markers are membrane bound and vesicles are as large as >3 μm diameter on average. Pixel based colocalization PCC is therefore not suitable and instead number of DNA containing compartment was counted. Percentage compartments containing both DNA nanodevice and bearing the membrane marker were calculated for targeting specificity.

RatiNa is localized to early endosome, late endosome and lysosome with high efficacy at 5 min, 17 min and 60 min respectively (Figure 15a). Next, we check off-target labeling by assessing anti-colocalization with other endocytic organelles. *RatiNa* is trafficked from early endosome to late endosome, so tested the extent of colocalization at 5 min with late endosomes. Indeed, there is <15% colocalization of *RatiNa* with RAB-7 at 5 min post injection (Figure 15b). Similarly anti-colocalization with early endosome was shown for late endosome labeling conditions. There is <15% colocalization of *RatiNa* with RAB-5 at 17 min post injection (Figure 15b). RAB-7 partially labels lysosome, so it is not a good marker for anti-colocalization. Therefore, we used LMP-1 anti-colocalization at 17 min to show specificity of lysosome targeting (Figure 15b).

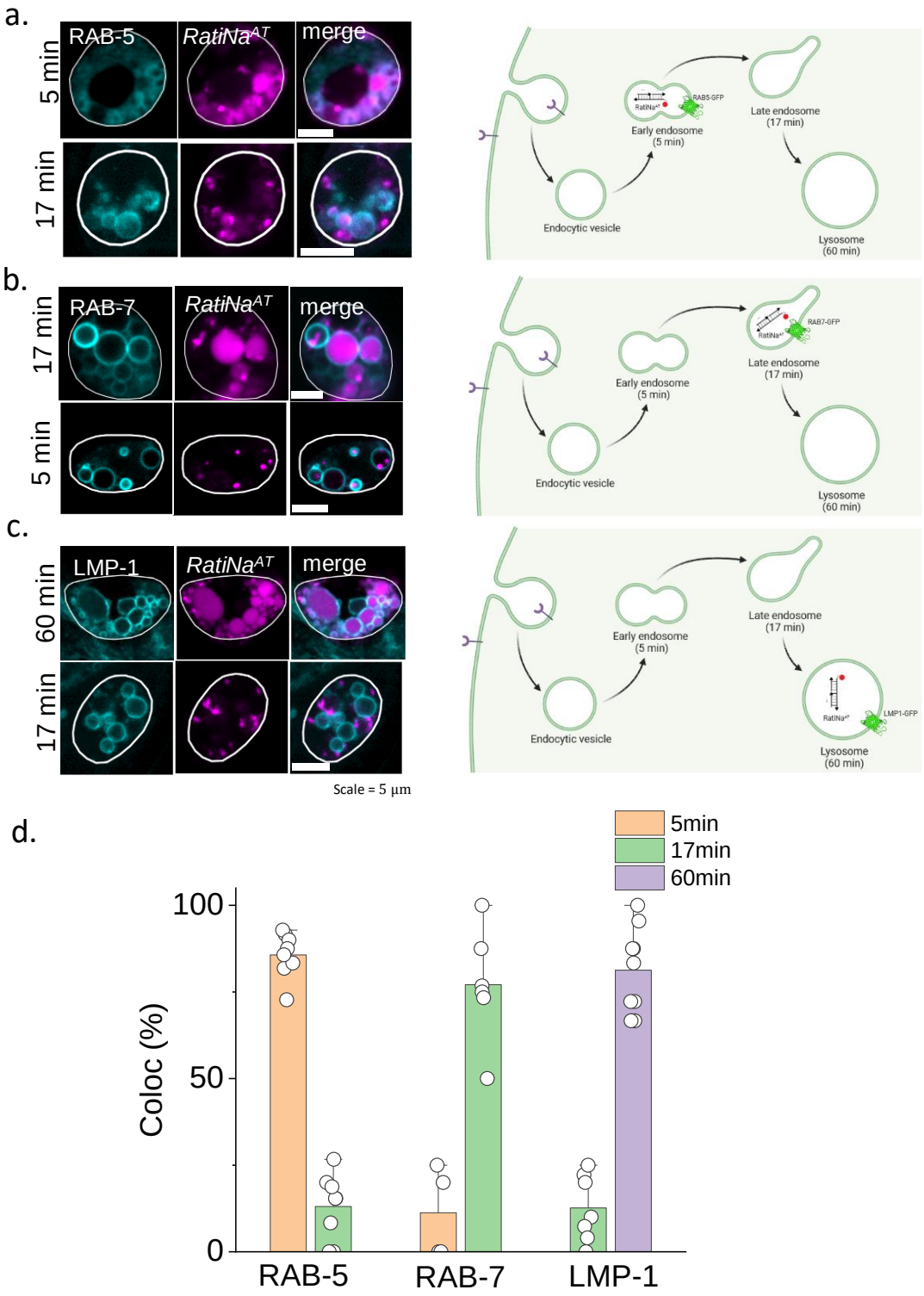

Figure 15. Targeting of C. elegans endocytic organelles. a. *RatiNa*^{AT} colocalization with early endosome and anti-colocalization with late endosome. b. *RatiNa*^{AT} colocalization with late

(Figure 15 Continued) endosome and anti-colocalization with early endosome. c. *RatiNa*^{AT} colocalization with lysosome and anti-colocalization with late endosomes. d. Quantification of targeting early endosome, late endosome and lysosome.

iii. *C. elegans* clamping and lysosome Na^+ measurement

Worms were punctured several times with injection needle and incubated with Na^+ clamping buffer for 1 h. The *C. elegans* clamping buffer has a pH of 5.5 and contains 150 mM Na^+ and K^+, 150 mM Cl-, 50 μM monensin, 50 μM nigericin, 10 μM gramicidin, 100 μM ouabain. The buffer mimics Na^+ and K^+ level in biological system: total amount of both cations is ~150 mM. Monensin is a Na^+ ionophore, nigericin is a K^+ ionophore, gramicidin can form ion-channel like pores in membranes to facilitate Na^+ and K^+ ion exchange via diffusion[77]. Ouabain inhibits Na^+/K^+ ATPase which actively transport Na^+ and K^+ to maintain high cytosolic K^+ and low cytosolic Na^+. We chose pH 5.5 because it's close to *C. elegans* lysosomal pH. Ionophores bind Na^+ or K^+ in their deprotonated forms and release bound ion when protonated. Having a steep pH gradient across lysosomal membrane makes the protonation and deprotonation cycle much better therefore pH 5.5 buffer is used.

Clamping of organellar Na^+ is challenging since the amount of Na^+ needs to be transported is on the millimolar scale. After one hour of clamping we observed a morphological change of *C. elegans* lysosomes from spherical to amorphous, and the effect is more severe when clamping at extreme values of 5 mM and 145 mM Na^+ (Figure 16b). We compared G/R values of clamped lysosomes and *RatiNa* beads and found that indeed G/R levels are very similar in both cases with slight shift in the extreme values of Na^+ (Figure 16c). Therefore, we used the bead data to extrapolate the *RatiNa* calibration curve in *C. elegans* since we reasoned that Na^+ levels for the

extreme values may not have been fully clamped (Figure 16d). *RatiNa* calibration curve is obtained for the physiologically relevant regime of Na^+ from 5 mM to 145 mM. Although on the logarithmic scale G/R values of *RatiNa* increases sigmoidally with Na^+, for the regime 5 mM to 145 mM it is approximately linear as shown both in bead and *C. elegans* clamping (Figure 12d, 16d).

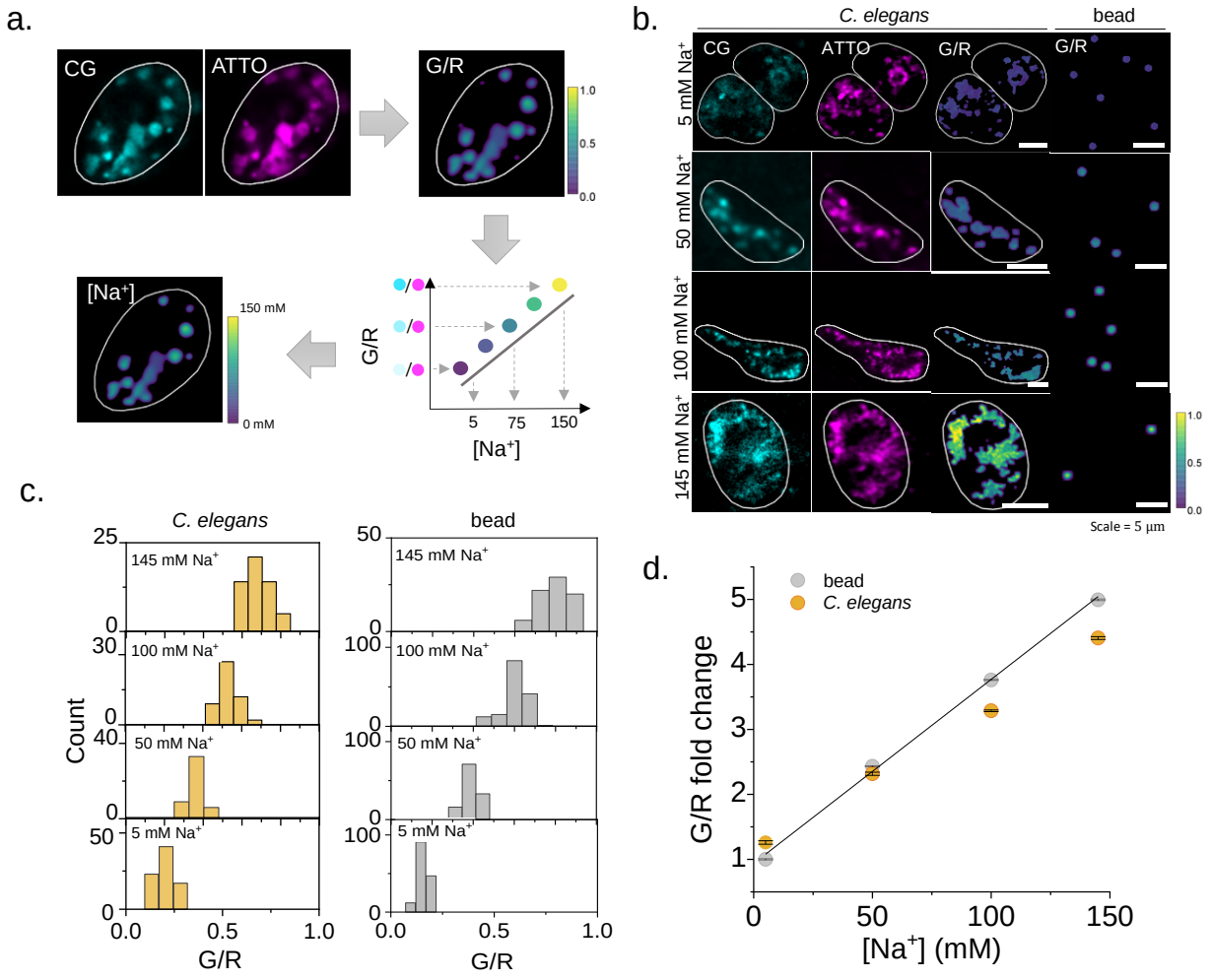

Figure 16. RatiNa clamping in vivo. a. Workflow of analysis of imaging data. First G/R image is generated from CG channel image (cyan) and ATTO channel image (maganta). Then the calibration curve of G/R to $[Na^+]$ is applied and G/R image is converted into a Na^+ heatmap. b. Ratiometric images of *RatiNa*^{biotin} on beads (right panels) and *RatiNa*-labeled, Na^+ clamped *C.*

(Figure 16 Continued) *elegans* lysosomes (left panels) at the indicated Na^+ levels. c. Histogram of G/R value of individual clamped lysosome and clamped bead (N > 80 per Na^+ level). d. Calibration curve is generated from averaged bead clamping data.

We chose lysosomes as our target organelle for initial investigations. dsDNA is naturally targeted to lysosomes for degradation as mentioned earlier. Further, lysosomes can also accumulate more nanodevices, which facilitates *RatiNa* imaging and measurement of Na^+. For *C. elegans*, lysosomes were labeled by microinjecting 2 μM of *RatiNa* in young adult N2 worms and imaged after 1 h chase time. Images were taken with the same settings for bead clamping and cell clamping: White light laser was set to 85% and 63x objective (Leica HC PL APO CS2 63x 1.40NA) and Hybrid detectors (Leica HyD X) were used. Sequential scan is used, and pinhole was set to 95.5 μm. For CG, the 522 nm laser was used for excitation (10% intensity) and emission was collected from 530 nm to 580 nm (HyD X2 Gain 100). For ATTO647N, 646 nm laser was used for excitation (2% intensity) and emission was collected from 655 nm to 780 nm (HyD X4 Gain 10).

For image analysis in *C. elegans*, lysosomes are selected manually in the ATTO channel, the rolling ball method was used for background subtraction and the G/R value of each endosome or lysosome is calculated by taking ratio of integrated intensity in CG channel and ATTO channel. The ROI file and G/R values of each lysosome were saved and converted to the Na^+ value using the equation corresponding to the calibration profile obtained for *RatiNa* from 5 mM to 145 mM. To show lysosomal Na^+ in a more direct and visible way, the Na^+ heatmap is generated from background subtracted images in CG and ATTO channels (Figure 16a). Linear fit equation of

G/R to Na^+ is applied using the Image Expression Parser function. The resulting image was pseudo colored with Vridis lookup table and the contrast was adjusted to fit the color scale. Each experiment was done in triplicate from injection to analysis and the data is plotted on a log scale. Numerical data was processed and plotted with Origin. For analysis, data points corresponding to the Na^+ value of a single endosome was represented as a hollow circle, color coded according to each of the three trials. The color of the filled circle corresponds to the mean value of all endosomes in the indicated trial. The line represents the average endosomal Na^+ overall, and the error bar reports 1 standard deviation.

iv. Targeting and integrity of *RatiNa* in lysosomes of RAW 264.7 macrophages

Macrophages express high level of scavenger receptor and will uptake dsDNA by endocytosis[71]. We chose RAW 264.7 macrophages to test *RatiNa* performance in lysosomes of mammalian cells. RAW 264.7 cells are virally transformed monocyte/macrophage-like cells derived from BALB/c mice[78]. We have previously targeted DNA devices to lysosomes of these cells using a 30 min pulse and 30 min chase protocol[79]. To accumulate even more *RatiNa* in lysosomes, we pulse *RatiNa*^{AT} for 2 h instead. This new protocol led to substantially better signal while preserving the localization of *RatiNa*^{AT} in lysosomes, where the latter were prelabeled with 0.5 mg/mL TMR dextran (Figure 16a). PCC value is calculated for each cell and plotted as CL sample. Pixel shift is done by translating ATTO image by 20 pixels in both X and Y axes and re-calculated to show that the high PCC values are not due to random colocalization (Fig 14b).

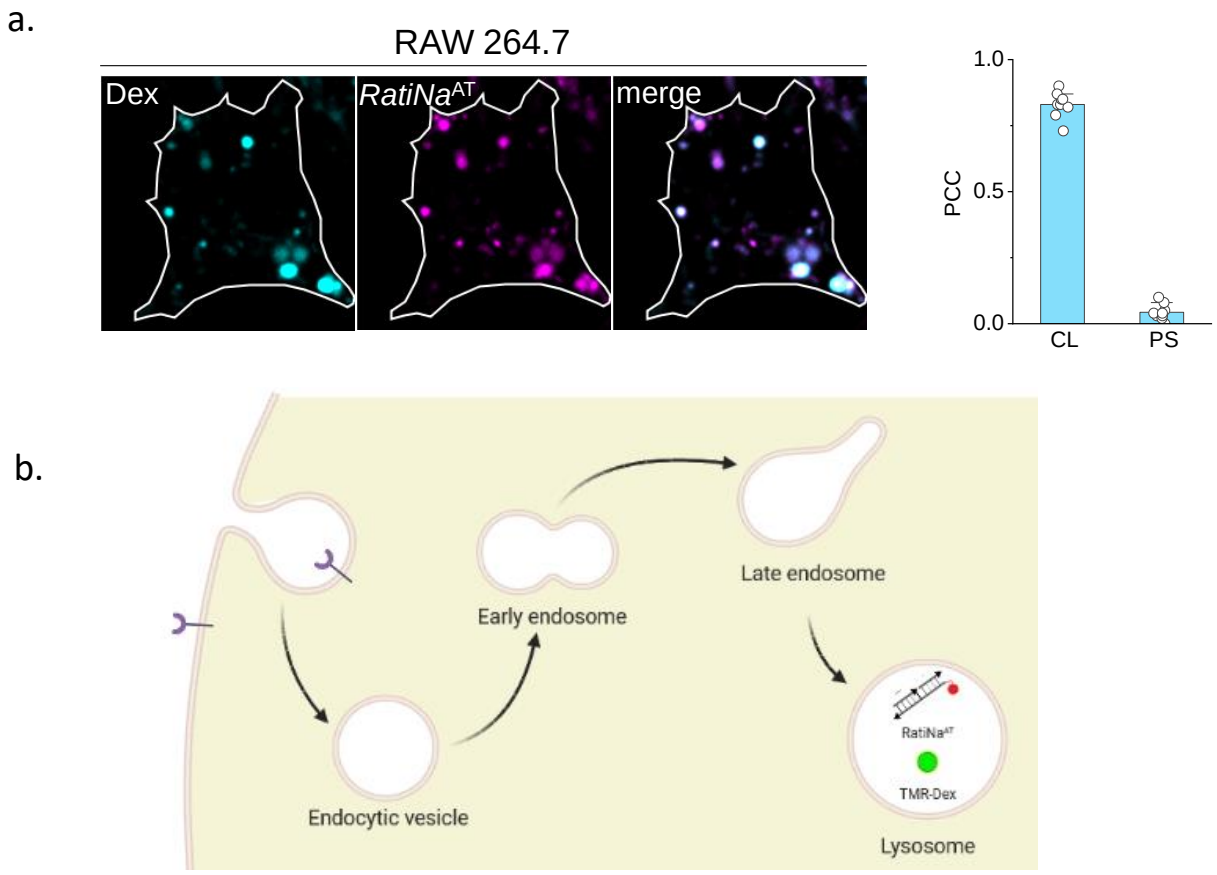

Figure 17. RatiNaAT targets RAW 264.7 lysosomes. a. RAW macrophages lysosomes targeting of *RatiNa*^{AT}. CL shows PCC value for colocalization, and PS shows PCC value for pixel shifted images for random colocalization. b. Illustration of *RatiNa*^{AT} and TMR-dex colocalization in lysosome created with BioRender.com.

Macrophage lysosomes are highly degradative and harbor several endonucleases and exonucleases[80]. Therefore, we need to test the integrity of the DNA backbone of *RatiNa* to estimate when degradation of *RatiNa* sets in. We first labeled lysosomes with TMR-dextran which is not digested by lysosomal enzymes. Then *RatiNa*^{AT} was targeted to lysosome with 2 h pulse and 30 min chase. The signal from TMR-dextran is expected to stay constant, while the red

signal from *RatiNa*^{AT} is expected to decrease as DNA degrades resulting in the free dye leaving the lysosome and thereafter the cytosol via diffusion across these biological membranes. Therefore R/G is a good indicator of DNA degradation. Indeed, we observe decrease of overall red signal (Figure 18a). We plotted the R/G signal of single lysosomes at different chase times (Figure 18b). The large spread of the R/G is due to differential uptake of dextran and DNA through fluid phase endocytosis and receptor mediated endocytosis respectively. But the R/G average indeed decreases. Previously we showed that for 30 min chase there is minimal DNA digestion. To better interpret the data, we use the following equation to calculate percentage of undigested DNA (Figure 18c):

$$Lysosomal\ DNA = \frac{(R/G)_t}{(R/G)_{t_0}} \qquad \text{Eq (2)}$$

where t = chase time and t_0 is 30 min. Based on this data, all subsequent studies did not measure Na+ in lysosomes beyond a 30 min chase time to ensure that *RatiNa* is fully intact.

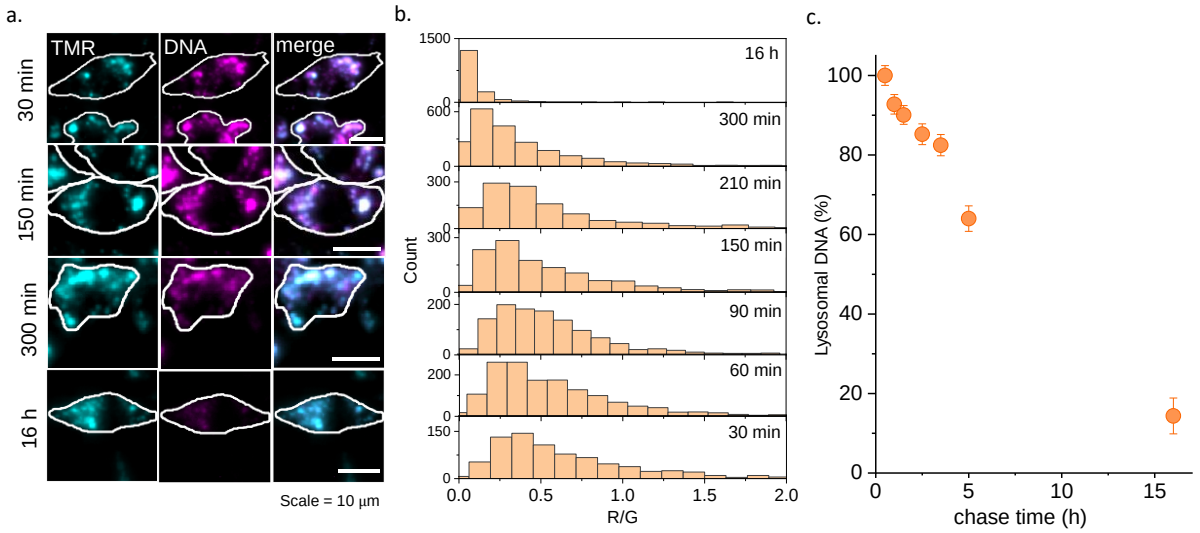

Figure 18. RatiNa is stable in RAW macrophages. a. Lysosomes in RAW264.7 macrophages labeled with TMR-dextran and *RatiNa*^{AT}, imaged at different chase times. b, Single lysosome

(Figure 18 Continued) R/G analysis shows *RatiNa*^{AT} is stable up to 3 h. c, DNA degradation as a function of chase time. Note that for 30 min chase time DNA is intact and ratiometry is valid. Error bar represents standard deviation

v. Na^+ measurement in lysosomes of RAW 264.7 macrophages

Unlike *C. elegans* coelomocytes which can accumulate almost all injected DNA in lysosomes, cultured cells uptake less DNA and the overall fluorescence signal is weaker. A new calibration curve is required for measurements in macrophage lysosomes. The clamping buffer we used for macrophage is pH 5.5, 150 mM Na^+ and K^+, 150 mM Cl^-, 5mM D-glucose, 1 mM $MgCl_2$, 1 mM $CaCl_2$, 10 mM HEPES, 50 μM monensin, 50 μM nigericin, 10 μM gramicidin, 100 μM ouabain[81]. The buffer is slightly different from *C. elegans* clamping buffer and better recapitulates the internal osmolarity of cultured cells, which prevent cells from swelling or shrinking while the internal cellular osmolarity equilibrates. Using a similar workflow I clamped macrophage lysosomes and attempted to image *RatiNa* in Na^+ clamped lysosomes. I noticed that CG signal is very low and G/R fold change from lysosomes is only ~2 fold compared to ~4 fold in *C. elegans* lysosomes.

To see whether *RatiNa* can reliably measure Na^+ in macrophage lysosomes, we investigated the difference of *RatiNa* fold change in macrophages. I observed that autofluorescence can be detected at the optimal excitation and emission wavelength of CG in macrophages (Figure 19a). Then I evaluated the contribution of *RatiNa*^{AT} in macrophages in both CG channel and ATTO channel and I observed signal in both channels. If the ROI is picked from ATTO channel and G/R is calculated for *RatiNa*^{AT} containing lysosomes, a non-specific G/R signal is obtained even without the CG dye (Figure 19b). If the average non-specific G/R signal is subtracted from G/R

from clamped lysosomes, the fold change of G/R signal now reaches ~3.5 from 5 mM to 145 mM Na^+, which is similar to *C. elegans* clamped lysosomes (Figure 19c, 19d). I concluded that even though the fold change is lower in macrophages due to their higher autofluorescence in the CG channel, we can still obtaine a calibration profile by Na^+ clamping. The new calibration profile then had to be used for all Na^+ measurements in lysosomes of RAW 264.7 macrophages.

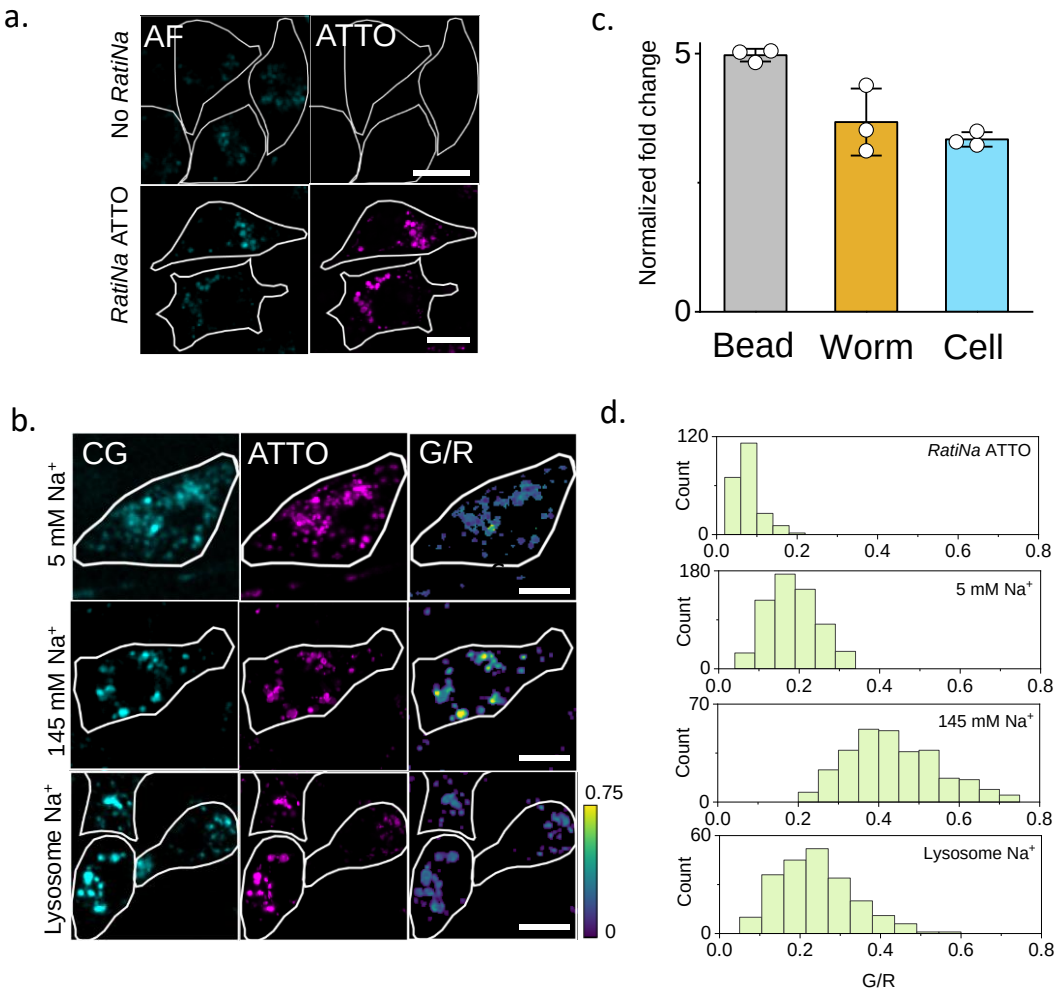

Figure 19. RatiNa clamping in RAW macrophages. a. Fluorescence images of *RatiNa*^{AT} labeled RAW264.7 macrophages in CG (G) and ATTO (R) channels. b. Comparison of fold change with *RatiNa* in bead and worm after correcting for non-specific signal. c. Images of

(Figure 19 Continued) *RatiNa*^{AT}-labeled lysosomes clamped at various indicated Na^+ and in native lysosomes. G/R heat maps show adequate change that Na^+ can be measured in native lysosomes. d. Distribution of G/R values of *RatiNa*-labeled single lysosomes. Accounting for autofluorescence, the fold change in G/R signal of *RatiNa* in lysosomes of RAW264.7 macrophages is comparable to that in *C. elegans* and on beads.

For Na^+ measurement in macrophage lysosomes, 1 μM *RatiNa* in prewarmed Opti-MEM was added to RAW 264.7 macrophages and incubated for 2 hours for maximum *RatiNa* uptake. Cells were then washed 3 times with PBS and incubated in prewarmed complete DMEM medium for 30 minutes to allow *RatiNa* to label lysosomes. Cells were then imaged in a confocal microscope (Figure 20a). White light laser was set to 85% and 63x objective (Leica HC PL APO CS2 63x 1.40NA) and Hybrid detectors (Leica HyD X) were used. Sequential scan is used, and pinhole was set to 95.5 μm. For CG 522 nm laser was used for excitation (30% intensity) and emission was collected from 530 nm to 580 nm (HyD X2 Gain 100). For ATTO647N, 646 nm laser was used for excitation (2% intensity) and emission was collected from 655 nm to 780 nm (HyD X4 Gain 10).

For image analysis single lysosomes are selected by a homemade Matlab program which picks out bright punctate ROI in images. Rolling ball method was used for background subtraction. G/R value of each endosome or lysosome is calculated by taking ratio of integrated intensity in CG channel and ATTO channel. ROI file and G/R value of each lysosome were saved and converted to Na^+ value using the equation of linear calibration curve from 5 mM to 145 mM. Three trials were done for each experiment and data is plotted on a log scale (Figure 20b). Numerical data was processed and plotted with Origin. For Na^+ measurement, data points of

single endosomes is represented as a hollow circle color coded according to each of the three trials. The filled circle represents the mean value of all endosomes in a given trial. The line represents the average endosomal Na^+ overall, and error bar reports 1 standard deviation.

Both in cultured cells and *in vivo*, lumenal Na^+ varies greatly across lysosomes. Our data revealed that Na^+ in single lysosomes in both systems could be as low as 5 mM or as high as 145 mM. However, on average across ~120 lysosomes, lysosomal Na^+ is ~43 mM Na^+ in *C. elegans* and was comparable to ~48 mM Na^+ in RAW 264.7 macrophages. This reconciles previous measurements of lysosomal Na^+, both lacking single lysosome resolution, that differed from each other by ~130 mM[21,82].

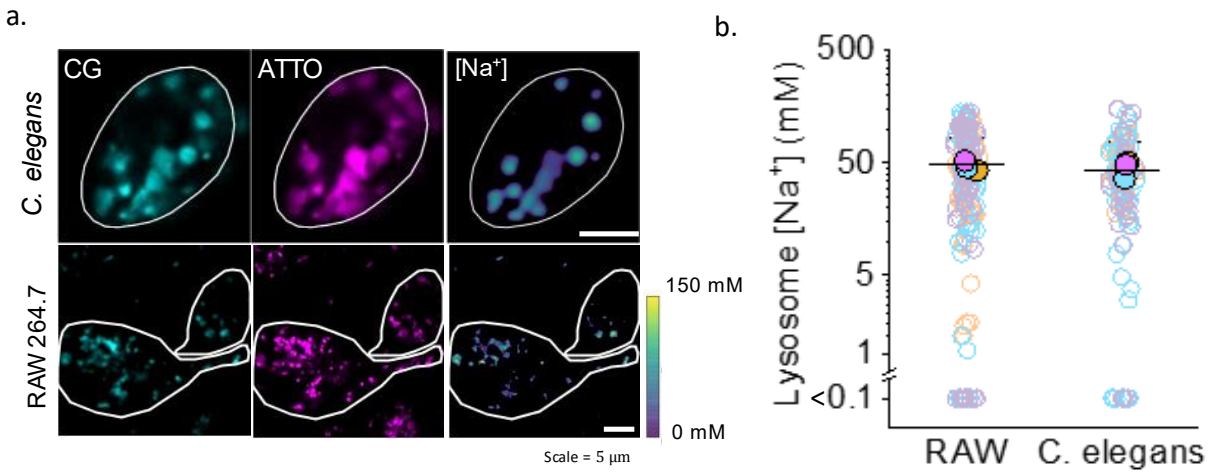

Figure 20. Lysosomal Na+ measurement. a. Representative images of *RatiNa* lysosome imaging. b. Lumenal Na^+ levels in single, native lysosomes in *C. elegans* and RAW macrophages (n ~120 lysosomes) performed in triplicate, with data from each trial color coded and the mean value of each trial given by a filled circle of the corresponding color.[83]

Chapter 3. *RatiNa* maps Na^+ in multiple organelles

i. *RatiNa* maps Na^+ in early and late endosomes of *C. elegans*

Until now I have demonstrated that *RatiNa* can map Na^+ in lysosomes of cultured cells and in a live organism. I observed that Na^+ levels vary greatly across single lysosomes, and that on average, it is ~40 mM in worms and nematodes. Next, we want to measure Na^+ in other organelles. Our group has previously targeted DNA nanodevices to different organelles including early endosomes[84], late endosomes[85], lysosomes[73], recycling endosomes[42], trans-Golgi networks[86], plasma membrane[86] and phagosomes[87]. Therefore, we can potentially target *RatiNa* to any of these organelles and measure Na^+. Our long-term goal is to get a complete picture of Na^+ levels in every kind of organelle. However, we first need to show that *RatiNa* can work in organelles other than the lysosome and show generalizability.

We know that early endosomes and late endosomes in *C. elegans* coelomocytes can be reliably targeted using *RatiNa*^{AT}. Using the same pulse and chase protocol we developed for *RatiNa*^{AT} targeting we used *RatiNa* to label early endosomes and late endosomes and measured Na^+ in these organelles. We found that early endosomes and late endosomes have ~74 mM and ~51 mM lumenal Na^+ respectively (Figure 21a). It is interesting to note that lumenal Na^+ decreases along the endocytic pathway because for every previously measured ion such as H^+, Cl^- and Ca^{2+}, the lumenal ionic level increases as a function of endosomal maturation (Figure 21b). However, Na^+ is highest in the early endosome, then decreases dramatically in the late endosome and thereafter shows a milder decrease in lysosomes.

One potential explanation is that since early endosomes forms immediately after endocytosis, the lumenal Na^+ level should be similar to extracellular milieu which has high Na^+. Although we do not know the precise Na^+ level in the pseudocoelom, it is very likely to match that of

mammalian and other organisms, and certainly exceed that within early endosomes. Our measurements reveal that there must be significant Na^+ efflux in early endosomes and late endosomes, but the transporters responsible for this efflux are yet to be identified.

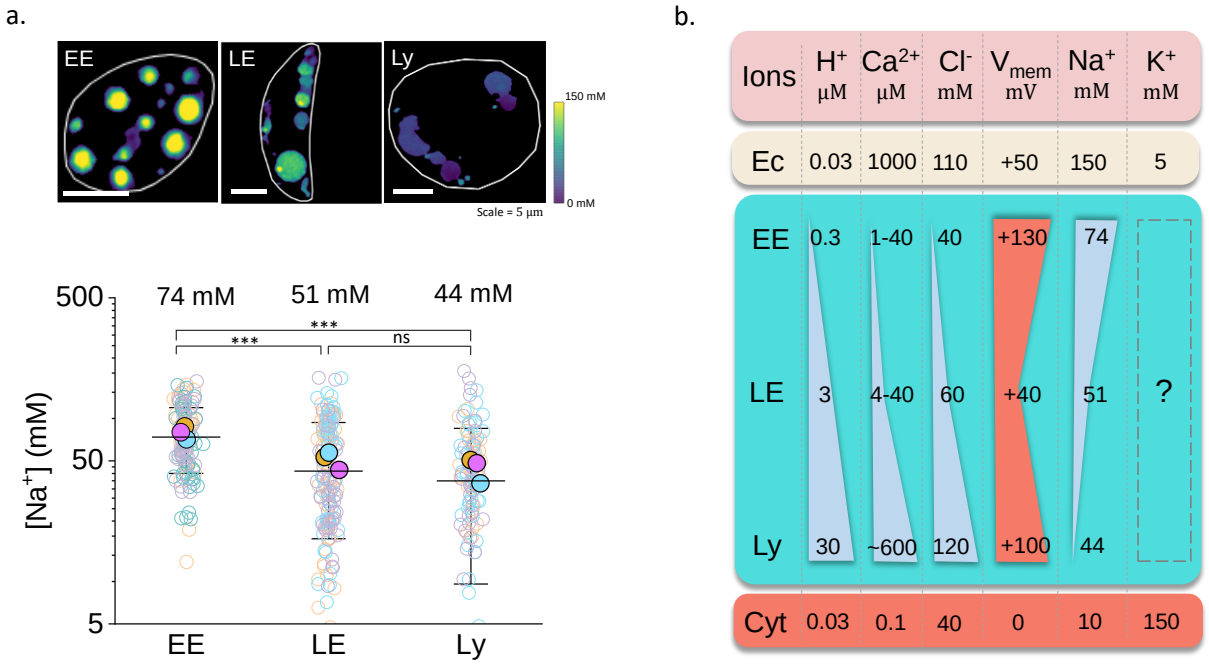

Figure 21. Na+ measurement in endocytic organelles in C. elegans. a. *RatiNa* maps lumenal Na^+ levels at each stage of endosomal maturation in coelomocytes of N2 *C. elegans* (n~130 endosomes per stage). Na^+ level is highest in early endosomes (EE) and falls as EE matures into late endosomes (LE) and lysosomes (Ly). b. Na^+ level as a function of endosomal maturation is plotted together with other ions and membrane potential. Ec: extracellular matrix. Cyt: cytosol.

ii. Measuring physiological perturbations of lysosomal Na^+ with *RatiNa*

So far, I have successfully measured Na^+ in early endosomes, late endosomes and lysosomes in their native states both *in cellulo* and *in vivo*. Beyond simply mapping organellar Na^+, another

crucial application of *RatiNa* is to test whether it can measure physiological perturbations of Na^+ levels in organelles. As stated previously, excessive Na^+ intake can lead to diseases and questions related to organelle involvement in these diseases, or whether perturbations in extracellular Na^+ are transferred downstream to organelles remain unknown. First, we need to test whether *RatiNa* can report changes in Na^+ levels in a single organelle. The lysosomal membrane harbors Na^+ channels such as Two Pore Channel 2 (TPC2), which is very well studied. In 2009 Zhu et al. reported that TPC2 is a lysosomal Ca^{2+} channel activated by NAADP[88]. Later, in 2012 Xu et al. reported that TPC proteins can also function as Na^+ channels when activated by lipid $PI(3,5)P_2$. TPC2 is exclusively on the lysosomal membrane and its activation should lower lumenal Na^+ since average lysosomal Na^+ of ~40 mM is higher than that of the cytosol which is ~10 mM. There are agonists and antagonists of TPC proteins but none of these small molecules selectively targets the Na^+ transport function of TPC proteins[89–92]. I treated RAW 264.7 macrophages with many of these reported agonists and antagonists and found no change in the equilibrium level of lysosomal Na^+ (Data not shown). It is possible that if lysosomal Ca^{2+} is also transported during TPC activation or inhibition, it could engage other Na^+ transporters in the lysosome and override the Na^+ transport due to TPC activity. To specifically activate Na^+ channels functionality of TPC2, I decided to target $PI(3,5)P_2$ which is an endogenous regulator of TPC Na^+ channel activity. PI(3)P is converted to $PI(3,5)P_2$ by the action of the kinase PIKfyve[93] (Figure 22a). Thus, PIKfyve inhibition is expected to reduce $PI(3,5)P_2$ levels and a previous report indeed demonstrates that PIKfyve inhibition can lead to inhibition of TPC proteins[94,95].

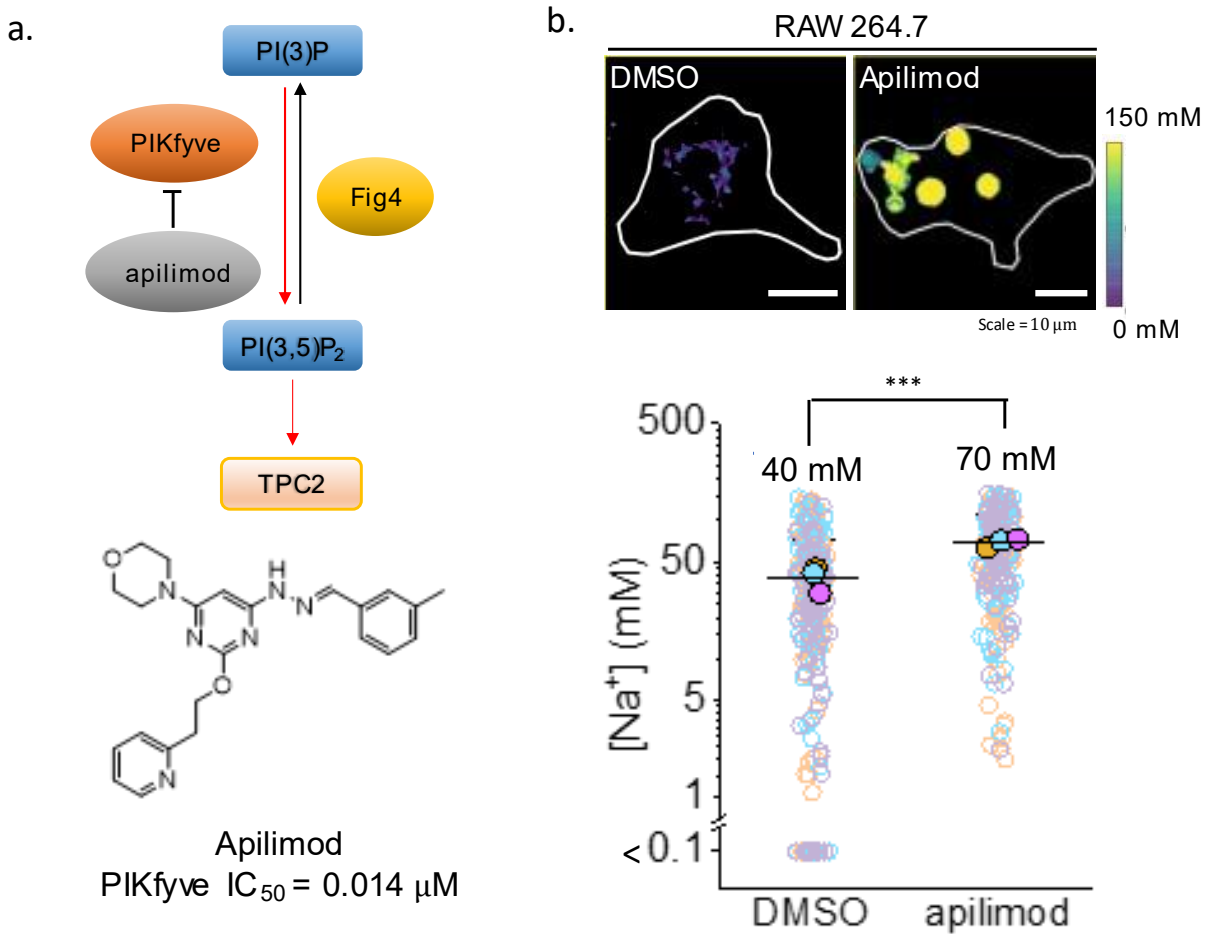

Figure 22. PIKfyve inhibition results in Na+ accumulation in lysosome via TPC2 inhibition.

a. Schematic of mode of action of apilimod inhibition of Na+ transport of TPC2 channels. Structure and IC50 of apilimod is also shown. b. RatiNa maps lumenal Na+ in lysosomes of RAW264.7 macrophages and upon inhibiting lysosomal Na+ channel, TPC2, with apilimod. (n~250 lysosomes). All experiments were performed in triplicate. Data from each trial are colour coded. Mean value of each trial is in filled circle of the corresponding colour83. * $P \leq 0.05$; ** $P \leq 0.01$; *** $P \leq 0.001$ by paired t-test.

I therefore treated RAW 264.7 macrophages with apilimod, a potent PIKfyve inhibitor, and measured lysosomal Na^+. Briefly, RAW 264.7 macrophage were treated with 100 nM apilimod (sigma SML2974) for 1 hour to inhibit PIKfyve. 1 μM of *RatiNa* was pulsed for 2 h and chased for 30 min with 100 nM apilimod in all medium. Cells were then imaged in a confocal microscope and lysosomal Na^+ was measured as previously described. Again, I observed enlarged lysosomes as previously reported[96]. This is caused by PIKfyve inhibition, which induces lysosomal fusion. Excitingly, I observed a dramatic increase of lysosomal Na^+ to ~70 mM due to TPC2 protein inhibition (Figure 22b). Note that $PI(3,5)P_2$ can also act on other lysosomal channels like TRPML1[97] and there can be other undocumented targets of $PI(3,5)P_2$ on lysosome that may also function as Na^+ channels. Importantly, the increase in lysosomal Na+ cannot be attributed to lysosomal fusion with other organelles, such as late endosomes or other lysosomes, because these would not elevate Na^+ to such high levels. Thus, this concentration change can be clearly attributed to a lack of Na^+ transporter in the lysosome. Clearly, *RatiNa* can indeed capture changes in lysosomal Na^+ due to physiological perturbations which can be broadly impactful. For one, we can use *RatiNa* to measure organellar Na^+ in disease states. Additionally, we can potentially discover new modulators of organelle Na^+ transport as well as new organellar transporters. These are exciting new directions with great possibilities for new discoveries.

iii. Considerations for how lumenal Na^+ affects organelle membrane potential

I hypothesize that lumenal Na^+ concentration in organelles can affect its membrane potential. Given what we know about organelle membrane potential and lumenal levels of ions in these organelles, I analyze below, how the values of organellar Na^+ determined in this thesis might affect membrane potential and potentially, further support our measurements of organellar Na^+.

The reversal potential for an ion is determined by the transmembrane concentration. Using the Nernst equation, we can derive the reversal potential for a positively charged ion:

$$E_{eq} = \frac{RT}{zF} ln \frac{[X^+]_{out}}{[X^+]_{in}} \quad \text{Eq. (3)}$$

Where R is the ideal gas constant, T is the absolute temperature, z is the number of elementary charges, F is the Faraday constant, $[X^+]_{out}$ is the ion concentration on the lumenal side (cytosol positive). $[X^+]_{in}$ is the ion concentration on the cytosolic side.

At physiological temperatures, i.e., 37 °C, I plot the reversal potential of Na^+ versus organellar lumenal Na^+ concentration as shown in Fig 23 below:

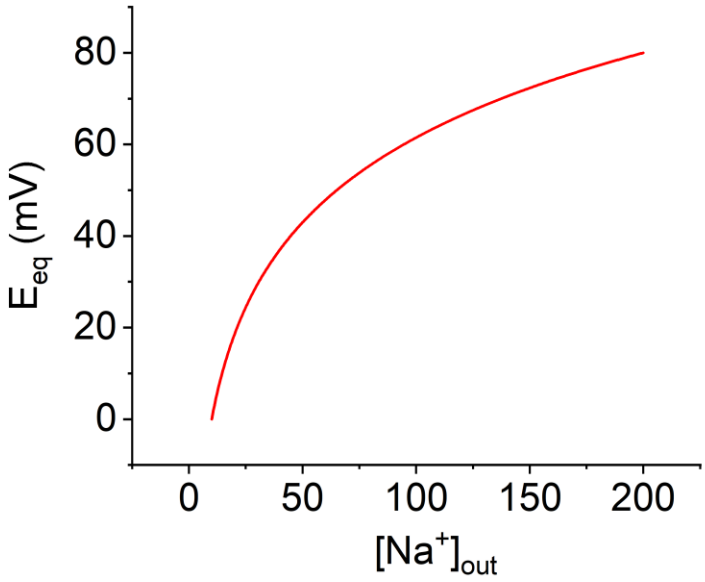

Figure 23. Lumenal [Na+] and its respective reversal potential. The reversal potential of Na^+ at a given organellar membrane can be plotted from Nernst equation. Here $[Na^+]_{out}$ is the lumenal concentration of Na^+ when considering organellar membrane.

From the Nernst equation, the reversal potential E_{eq} can be plotted for Na^+. Note that for organelles, lumenal Na^+ concentration is equivalent of $[Na^+]_{out}$ for plasma membrane.

$$E_{eq,Na^+} = 61.5\ mV\ \times \log\left(\frac{[Na^+]_{out}}{[Na^+]_{in}}\right) \quad \text{Eq. (4)}$$

For a cytosolic Na^+ concentration of 10 mM, and experimentally determined lumenal concentrations of 74 mM, 51 mM and 44 mM for early endosomes, late endosomes and lysosomes respectively, the reversal potential of Na^+ is estimated at +53 mV, +44 mV and +40 mV. To relate lumenal Na^+ concentration to the resting membrane potential, Goldman-Hodgkin-Katz voltage equation can be used and we can consider the resting potential for an organelle to be given by:

$$E_m = \frac{RT}{F}\ln\frac{P_{Na}[Na^+]_{out}+P_K[K^+]_{out}+P_{Cl}[Cl^-]_{in}}{P_{Na}[Na^+]_{in}+P_K[K^+]_{in}+P_{Cl}[Cl^-]_{out}} \quad \text{Eq. (5)}$$

where P_{Na}, P_K and P_{Cl} to be the selective permeabilities for Na^+, K^+ and Cl^- respectively. Here we did not consider H^+ and Ca^{2+} since their concentration is in micromolar range, suggesting that their contributions are likely to be comparatively insignificant. If we use the measured values of absolute membrane potential of the early endosome, late endosomes or lysosome as +130 mV, +40 mV and +100 mV, then for the early endosome:

$$E_{m,EE} = \frac{RT}{F}\,ln\frac{P_{Na}[Na^+]_{lumen}+P_K[K^+]_{lumen}+P_{Cl}[Cl^-]_{cyt}}{P_{Na}[Na^+]_{cyt}+P_K[K^+]_{cyt}+P_{Cl}[Cl^-]_{lumen}} \quad \text{Eq. (6)}$$

$$\frac{74mM\ P_{Na}+P_K[K^+]_{out}+40mM\ P_{Cl}}{10mM\ P_{Na}+150mM\ P_K+40mM\ P_{Cl}} = 130\ AU \quad \text{Eq. (7)}$$

Early endosomes are highly hyperpolarized, and we have no clear idea of the ion permeability of this organelle membrane due to the paucity of knowledge of ion transporters in this organelle. To achieve and maintain such high membrane potentials, the permeability of Na^+ must be very high

and accordingly, the Na^+ gradient is highest across the early endosome membrane. This is further supported by the rapid drop of Na^+ levels as endosomes mature from early endosome to late endosome. My labmate, Dr Palapuravan Anees, has measured K^+ level in early endosome to be ~ 20 mM (unpublished) which is much lower than cytosolic K^+ (150 mM). This suggests that permeability for K^+ should be lower than Na^+ or $P_{Na} > P_K$ in the early endosome.

For late endosomes, using the values for membrane potential and ion concentration, we obtain:

$$E_{m,LE} = \frac{RT}{F} ln \frac{P_{Na}[Na^+]_{lumen} + P_K[K^+]_{lumen} + P_{Cl}[Cl^-]_{cyt}}{P_{Na}[Na^+]_{cyt} + P_K[K^+]_{cyt} + P_{Cl}[Cl^-]_{lumen}} \quad \text{Eq. (8)}$$

$$\frac{51mM\ P_{Na} + P_K[K^+]_{out} + 40mM\ P_{Cl}}{10mM\ P_{Na} + 150mM\ P_K + 60mM\ P_{Cl}} = 4.5\ AU \quad \text{Eq. (9)}$$

The late endosome has much less membrane potential than early endosomes. Here too, the permeability for ions is obscure due to the lack of knowledge of ion transporters. The K^+ level in the late endosome is currently unknown. Focusing on the Na^+ term in equation (9), we see that change in lumenal Na^+ levels is much less compared to change in membrane potential. This is further supported by the reversal potential change of +53 mV to +44 mV from early endosome to late endosome. Therefore, the decrease in lumenal Na^+ alone is not sufficient to explain the change of membrane potential. I therefore posit that the permeability of Na^+ in the late endosome is lower than in the early endosome. I further posit that the membrane potential of the late endosomes is also heavily affected by lumenal K^+ levels and permeability of K^+ and Cl^-. These values are yet to be measured.

For lysosomes, we use the values for membrane potential and ion concentration as follows:

$$E_{m,Ly} = \frac{RT}{F} ln \frac{P_{Na}[Na^+]_{lumen} + P_K[K^+]_{lumen} + P_{Cl}[Cl^-]_{cyt}}{P_{Na}[Na^+]_{cyt} + P_K[K^+]_{cyt} + P_{Cl}[Cl^-]_{lumen}} \quad \text{Eq. (10)}$$

$$\frac{44mM\ P_{Na}+P_K[K^+]_{out}+40mM\ P_{Cl}}{10mM\ P_{Na}+150mM\ P_K+120mM\ P_{Cl}} = 42\ AU \qquad \text{Eq. (11)}$$

Lysosomes, like early endosomes, are highly hyperpolarized. The transmembrane gradient of Na^+ is least for this organelle yet the membrane potential is high. Note that the reverse potential for Cl^- is -30 mV which counteracts the reversal potential for Na^+ at +40 mV. I hypothesize that the above model for monovalent ions may not be suitable to describe lysosomal resting membrane potential given the high transmembrane gradient for H^+ and Ca^{2+}. Additionally, experiments by Dr. Saminathan have revealed that H^+ transport across the lysosomal membrane accounts for ~90% of its membrane potential[20]. Thus, I conclude that ions other than Na^+, which have a high transmembrane gradient are the major contributors to the lysosomal membrane potential.

Thus, the Na^+ concentration changes observed at each endocytic stage clearly supports how the membrane potential profile of these organelles changes during endosomal maturation. However, the contribution of Na^+ alone is insufficient to explain the large change in membrane potential: Na^+ reversal potential goes from +40 mV in late endosomes to +53 mV in early endosomes, but the organelle membrane potential goes from +40 mV to +130 mV. Hence, the permeability for ions must be different from that across the plasma membrane where, for example in neurons, K^+ is far more permeable than either Na^+ or Cl^-. Organelle membranes harbor ion transporters with different mechanism and relative abundances. At this stage, due to the lack of knowledge of different transporters on organelle membranes we cannot comprehensively relate membrane potential with the resting transmembrane ion gradient. In lysosomes, where the Na^+ reversal potential is barely counteracting the Cl^- reversal potential, other abundant ions like H^+, Ca^{2+} and unknown charged ions such as polyamines may contribute to the high membrane potential of +100 mV.

Chapter 4. Lysosomes enable salt adaptation in *C. elegans*

i. *C. elegans* salt adaptation and brood size assay

C. elegans have a mechanism that senses the environmental salt levels for its optimal growth. In low salt conditions *C. elegans* is attracted to Na^+ and the ASE neurons are responsible for Na^+ chemotaxis behavior[98]. *C. elegans* also avoids high concentrations of Na^+ which requires *tmc-1* in ASH neurons[99]. While environmental salt levels are important for the optimal growth of nematodes, *C. elegans* are capable of adapting to high salt levels in the environment. Upon exposure to high salt, the worm experiences a hypertonic shock and loses body volume as water leaves[100]. The WNK pathway is activated and NKCC1 is activated by phosphorylation[101]. NKCC1 is a $Na^+/K^+/Cl^-$ cotransporter and Na^+ influx then allows the acute recovery of body volume[102]. Upon prolonged exposure to high Na^+, the glycerol synthesis pathway is activated, because glycerol serves as an osmolyte that increases the internal osmolarity to combat the hypertonic environment[100]. However, there is no evidence so far that organelles participate in the process of salt adaptation in animals, even though in plants vacuoles are known to handle excessive salt[103].

To investigate salt adaptation in *C. elegans*, we first established an assay for adaptation in our hands. We followed a previously published protocol to adapt *C. elegans* to high Na^+[100]. In brief, high Na^+ containing plates were made by supplementing NaCl to NGM plates (51 mM NaCl for normal NGM plate, 200 mM, 300 mM and 400 mM NaCl for high Na^+ plates). High Na^+ plates are sealed with parafilm and kept at 4°C until use. For adaptation, gravid worms were transferred to 200 mM Na^+ plate. Hatched worms were allowed to grow on 200 mM Na^+ plate for adaptation. Worms grown to the L4 embryonic stage are considered adapted to Na^+. As previously published, a live-or-dead assay can be used to score adaptation since only adapted

worms survive in 400 mM Na^+ plates. We too observed that adapted worms show normal physical activity in 400 mM Na^+ plates while unadapted worms do not move even though they are still alive and will respond if poked with a platinum wire. Therefore, we used brood size to score for salt stress on worms. Worms affected most by high Na^+ do not produce progeny while only those that have successfully adapted to high Na^+ lay egg and produce progeny.

For the brood size assay, 5 untreated (or adapted) worms are transferred to 200 mM, 300 mM and 400 mM Na^+ plate at L4 stage. Worms were allowed to lay eggs for 24 hours and removed from the plate. Progeny were allowed to grow for another 48 hours for easier visualization. Plates were photographed and brood size was counted (Figure 24). We were able to recapitulate the previous finding that *C. elegans* adapts to high Na^+ and can breed even in lethal amounts of Na^+ (Figure 24).

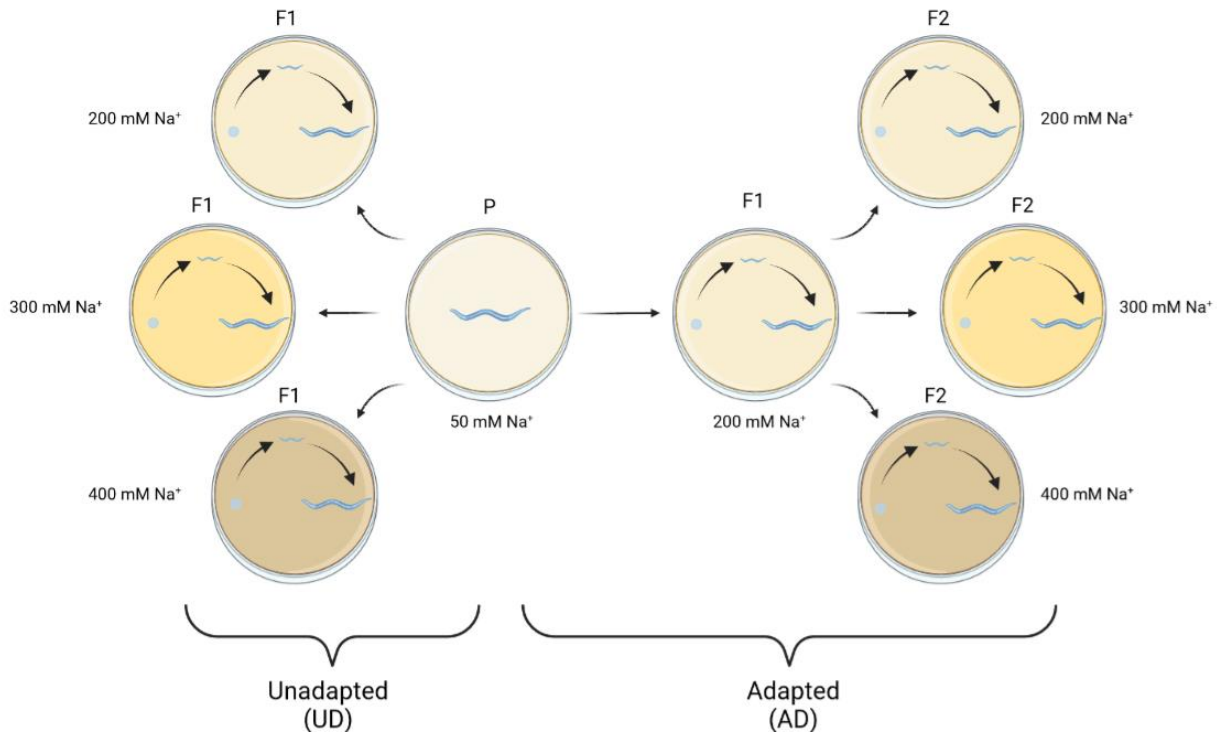

Figure 24. Schematic of C. elegans brood size assay. Brood size assay was designed to compare salt adaptability from different genetic backgrounds. For unadapted worms (UD), worms were directly transferred to high Na^+ plates from NGM plate and brood size were counted. For adapted worms, adaptation was done by allowing worms to grow for one generation at 200 mM Na^+ plate. Then adapted worms were transferred to high Na^+ plate and brood size were counted.

To address whether organelles participate in salt adaptation process, we tested the salt adaptation ability of worms lacking various Na^+ transporters either at the plasma membrane or in organelles. There are very few reports of organellar Na^+ transporters in *C. elegans*, and most relate to the NHX protein family. These are Na^+/H^+ exchangers and they have been previously shown to localize to intracellular compartments, even though the precise organelle is not

determined[104]. NCX proteins are Na^+/Ca^{2+} exchangers that are predominantly found on plasma membrane[105]. We used deletion mutants of *nhx* gene and *ncx* gene with following genetic background:

ok661 is a deletion mutant with 1411 bp deletion in nhx-5 gene (F57C7.2) and does not express NHX-5 globally. We will use ΔNHX-5 worm to refer to this deletion mutant.

ok583 is a deletion mutant with 1702 bp deletion in nhx-7 gene (K09C8.1) and does not express NHX-7 globally. We will use ΔNHX-7 worm to refer to this deletion mutant.

ok549 is a deletion mutant with 1584 bp deletion in nhx-8 gene (Y18D10A.6) and does not express NHX-8 globally. We will use ΔNHX-8 worm to refer to this deletion mutant.

gk879849 is a substitution mutant R634 to stop codon in ncx-2 gene (C10G8.5). We will use ΔNCX-2 worm to refer to this deletion mutant.

We found that, even after adaptation, all Na^+ mutants are more susceptible to salt stress than N2 worms (Figure 25). This may be because the Na^+ homeostasis machinery may require the activity of all these different Na^+ transporters and deleting any of them will render the worm less resistant to high environmental Na^+.

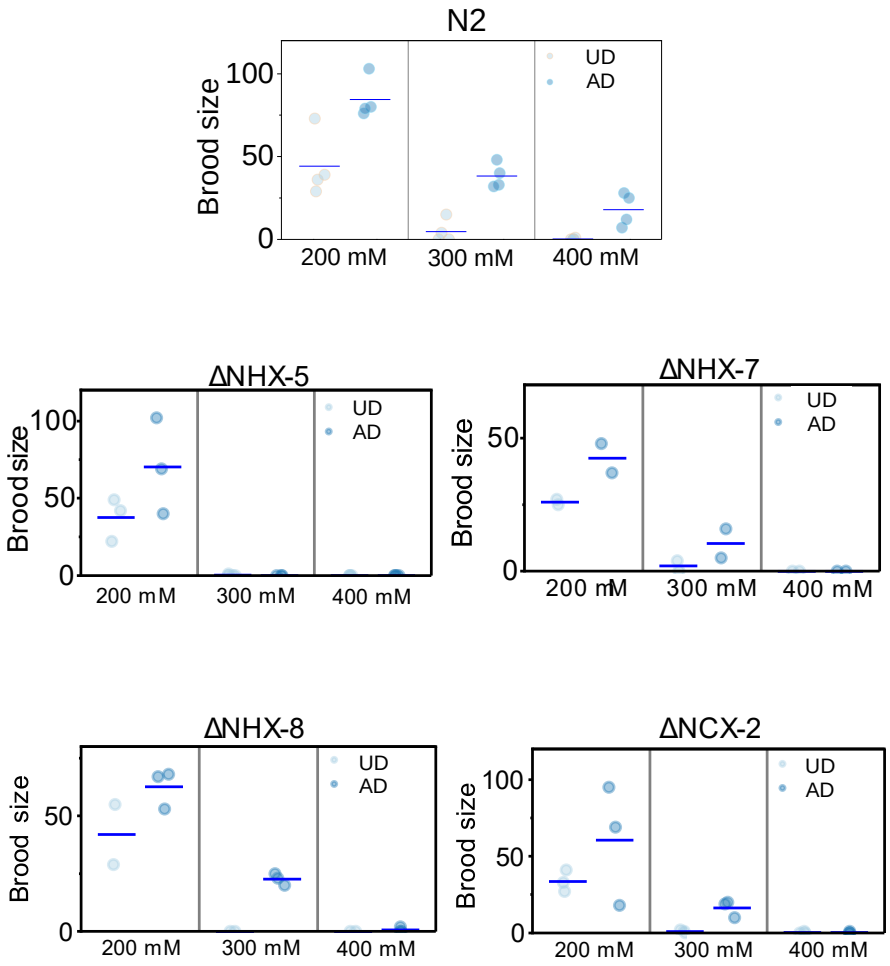

Figure 25. Adaptation of C. elegans to high Na+, given by brood size. Adaptability of *C. elegans* to high Na^+ was scored by brood size (N=3). Note that all adapted worms (AD) make more progeny compared to untreated worms (UD). Adapted N2 worms can tolerate up to 400 mM Na^+ and **Δ**NHX-5 mutant worms cannot tolerate even 300 mM Na^+.

ii. Organellar Na^+ levels in Na^+ transporter mutants

I then measured lysosomal Na^+ in the mutant worms. Similar to the perturbation in RAW 264.7 macrophages, I expect to find steady state levels of lysosomal Na^+ changed so as to reflect the

loss of activity due to transporter deletion. However, the results proved more interesting as they were less straightforward (Figure 26a, 26b). Lysosomal Na+ measurements revealed that ΔNHX-5 worms showed the lowest Na^+ levels of all the mutants. This indicates that NHX-5 may directly or indirectly facilitate lysosomal Na^+ import. The closest homolog of worm NHX-5 is human NHE9 (40% identity, 61% similarity, aligned with 90% sequence coverage), which, in humans mainly localizes to late endosomes and is expected to import Na^+ [106]. ΔNHX-7 worms have slightly lower lysosomal Na^+ but not as low as ΔNHX-5 worms. The closest homolog of worm NHX-7 is human NHE1 (35% identity, 55% similarity, aligned with 77% sequence coverage), which is a plasma membrane Na^+/H^+ exchanger. Similarly, ΔNCX-2 worms show slightly lesser lysosomal Na^+ but not as low as ΔNHX-5 worms. The closest homolog of NCX-2 is human NCX2 (45% identity, 63% similarity, aligned with 57% sequence coverage), which is found on plasma membrane (Figure 26c). The lysosomal Na+ level of ΔNHX-8 worms is unaffected compared to N2 worms. Its closest homolog is NHE8 (48% identity, 69% similarity, aligned with 61% sequence coverage), which is found mainly in TGN.

a.

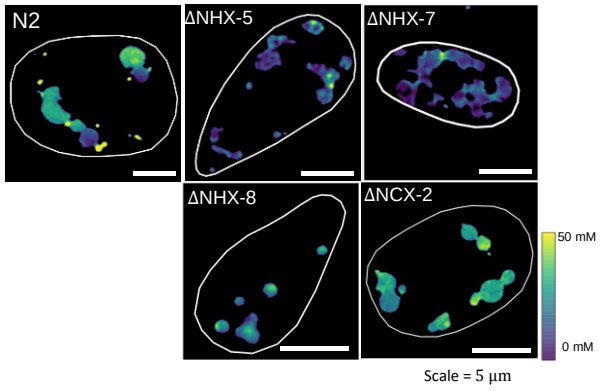

b.

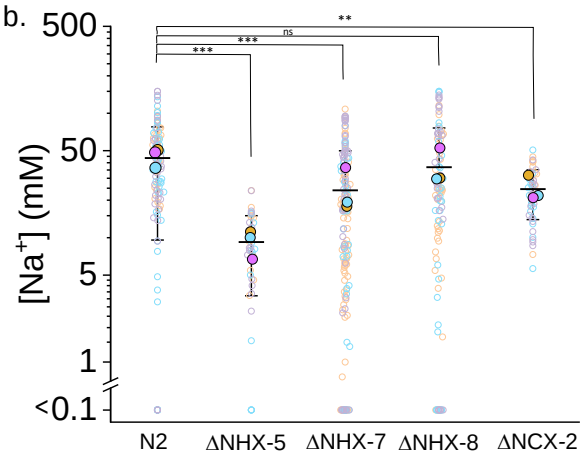

c.

C. elegans protein	Human protein	Identity/similarity	Predicted location
NHX-5	NHE9	40%/61%	Late endosome
NHX-7	NHE1	35%/55%	Plasma membrane
NHX-8	NHE8	48%/69%	Golgi
NCX-2	NCX2	45%/63%	Plasma membrane

Figure 26. Lysosomal Na+ measurement in Na+ transporter deletion mutants. a. Representative Na^+ heatmaps of WT and Na^+ transporter deletion mutant worms. b. Lumenal Na^+ levels in single lysosomes in worms of the indicated genetic background. (N = 120, 50, 170, 120, 60 for N2, **Δ**NHX-5, **Δ**NHX-7, **Δ**NHX-8, **Δ**NCX-2 respectively) For statistical analysis paired t-test is used and *, **, *** represents $P \leq 0.05, 0.01, 0.001$ respectively. c. Homology analysis of *C. elegans* genes investigated. Human analog can be used to infer about the subcellular location of NHX proteins.

Our results suggest that even if NHX-8 transports Na^+ in Golgi, it is unable to directly or indirectly toggle Na^+ transport in lysosomes. On the other hand, NHX-7 and NCX-2 transport Na^+ across plasma membrane and this loss of Na^+ transport can reduce lysosomal Na^+ , possibly

because it lowers cytosolic Na^+. ΔNHX-5 mutant has the lowest lysosomal Na^+ indicating that it directly or indirectly influences Na+ import in this organelle, given that the human homolog imports Na^+ in late endosomes. Notably ΔNHX-5 mutants were the least able to adapt to high salt.

iii. The bidirectionality of Na^+ exchangers enables salt adaptation

To understand how the regulation of organellar Na^+ connect to an organism level phenotype such as salt resistance, I measured lysosomal Na^+ in adapted N2 and mutant worms. I observed that intriguingly, post-adaptation, lysosomal Na^+ levels in N2 worms decreased. In contrast, in adapted mutant worms lysosomal Na^+ levels increased. This indicates that first, lysosomal Na^+ level changes as worms adapt to salt stress revealing that lysosomes support the adaptation process by modulating how they mobilize Na^+ (Figure 26).

We hypothesize that observed increase in lysosomal Na^+ in mutant worms upon adaptation is likely due to the exchanger changing its direction of transport during stress. During high Na^+ stress, the organelle may respond by exporting more Na^+ into cytosol so as to counter the high Na^+ coming into lysosomes via endocytosis. In an effort to restore lysosomal Na^+ to its normal levels, I posit that, in N2 worms, lysosomal Na^+ exchangers changes their directionality from one of Na^+ import to export. Worms that have adapted to salt stress have vigorous lysosomal Na^+ export as revealed by the lower steady state level of lysosomal Na^+ (Figure 27). A similar mechanism is seen in yeast where vacuolar NHX-1 activity required to survive high Na^+ stress[25]. This hypothesis is supported by our results from the NHX-5 deletion mutant. This mutants cannot export the excess lysosomal Na^+ and the adapted worms show a net increase of lysosomal Na^+ (Figure 26). This effect is so prominent that lysosomal Na^+ increases in all NHX mutants,

even plasma membrane Na^+/Ca^{2+} exchanger NCX-2 mutants. Our explanation is that impairing plasma membrane Na^+ export elevates cytosolic Na^+. This leads to lysosomal Na^+ transporters importing the excess Na^+ in order to eject it from the cell by lysosomal exocytosis.

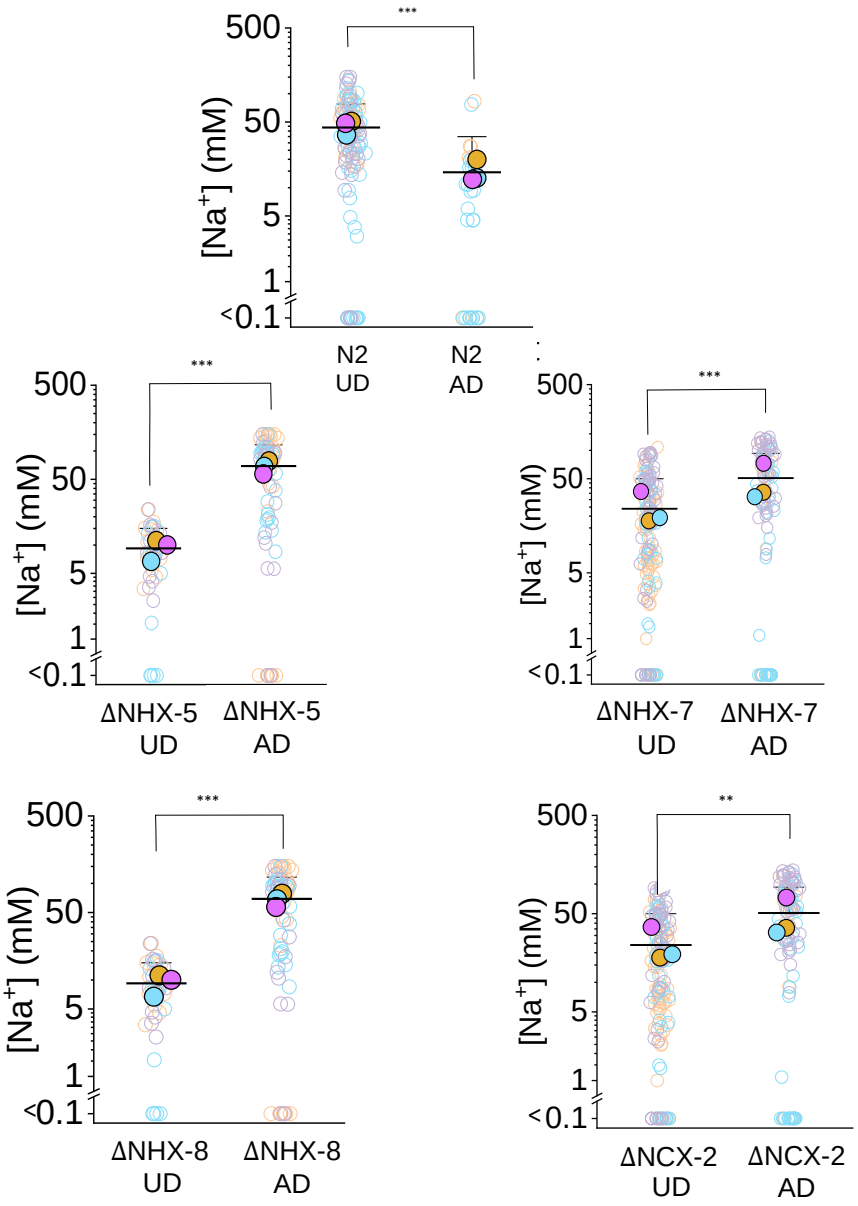

Figure 27. Lysosomal Na+ measurement in adapted Na+ transporter mutant worms.

Single lysosomal measurements of untreated and adapted lysosomal Na^+ (N > 120 for all adapted worms). Note that adapted N2 worms have lower lysosomal Na^+ whereas all mutant adapted

(Figure 27 continued) worms have higher lysosomal Na^+. For statistical analysis paired t-test is used and *, **, *** represents $P \leq 0.05, 0.01, 0.001$ respectively.

iv. Expression level of Na^+ transporter is unaltered in adapted worms

One of the possible reasons that lysosomal Na^+ changes upon adaptation is that salt adaptation may change the expression of Na^+ transporter genes which changes transporter activity and thus, the steady state levels of lysosomal Na^+. We therefore compared the expression levels of *nhx* and *ncx* genes in N2 worms pre and post adaptation by qRT-PCR (Figure 28). In brief, >50 adult worms are washed with M9 buffer twice and collected by centrifuging at 1,000 x g for 1 min. Aspirate off M9 and add 500 μL Trizol (Thermo 15596026) to the worm. The tube was then flash frozen with liquid N2 and thawed with 37 °C heat block 5 times followed by 1 min centrifugation at 3,000 x g. The supernatant was transferred to a new tube and 100 μL chloroform was added, vortexed the aqueous layer was left to separate from organic layer. The aqueous layer was collected and 250 μL of cold isopropanol was added. The mixture was incubated at room temperature for 5 min and -20°C for 1 hour, centrifuged at 12,000 x g for 10 min at 4°C and the supernatant discarded. The RNA pellet was washed with 500 μL cold 70% EtOH and centrifuged at 12,000 x g for 10 min. All the EtOH was removed by carefully pipetting out the supernatant and the pellet was air-dried with clean N_2. The RNA was resuspended in 30 μL RNAse free water.

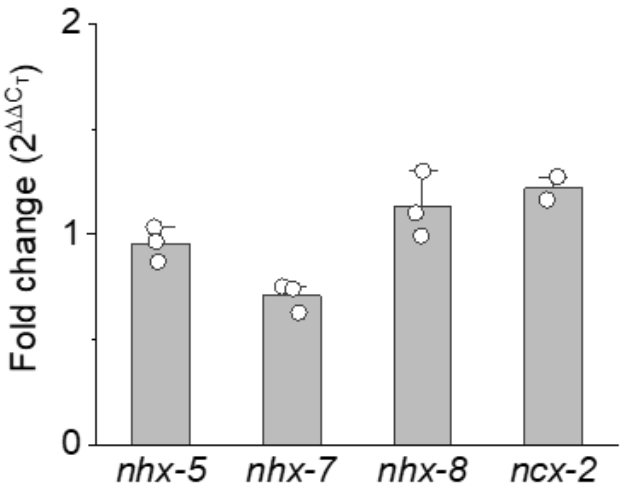

Figure 28. Comparison of gene expression levels of Na+ transporters in worms upon adaptation. Expression level of *nhx-5* and *ncx-2* mRNAs is similar in untreated and adapted N2 worms by qRT-PCT analysis. Fold change in mRNA levels of adapted worms compared to untreated worms was calculated from **ΔΔ**Ct. *Act-1* was used as reference gene.

cDNA was synthesized with Maxima H Minus cDNA synthesis master mix (Thermo, M1661) according to manufacturer's protocol. qPCR was performed with Roche LightCycler 96. ΔΔCT was used to calculate fold change difference of RNA level compared to control gene *act-1*. Following primers were used for qRT-PCR:

NHX-5 fwd: CGT CAA CTG TAG CAG GTT CTA A

NHX-5 rev: GGA AAC GTA GGT GAG GAG TAT G

NHX-7 fwd: GGA GCT TTA CCA CAC GAC TTA T

NHX-7 rev: GTG CAT GAG CTG ACG AAT AGA

NHX-8 fwd: CCA TCG TTC AAC TCG TTA CCT

NHX-8 rev: GAG CAA TGC ACT CAA CAA TCC

NCX-2 fwd: GAT TGA TCG GAG GAG GAG ATA TTG

NCX-2 rev: GTA GTG AGC TGG ATC CAA GAA G

ACT-1 fwd: CGA GCG TGG TTA CTC TTT CA

We found that the adaptation process didn't affect the mRNA level of investigated genes (Figure 28), further supporting that lysosomal Na^+ change is due to actual directional change of the Na^+ exchangers.

v. Lysosomes play a crucial role in worm Na^+ adaptation

To test whether the adaptation process was specifically supported by lysosomes, or generally by all endocytic organelles, we mapped lumenal Na^+ along the endolysosomal pathway in adapted N2 worms. We found that Na^+ levels in early endosome, late endosome and lysosomes were all lowered upon adaptation. However, the effect was most pronounced in lysosomes which showed ~67% decrease (Figure 29). Again, lysosome seem to be crucial for the adaptation to Na^+.

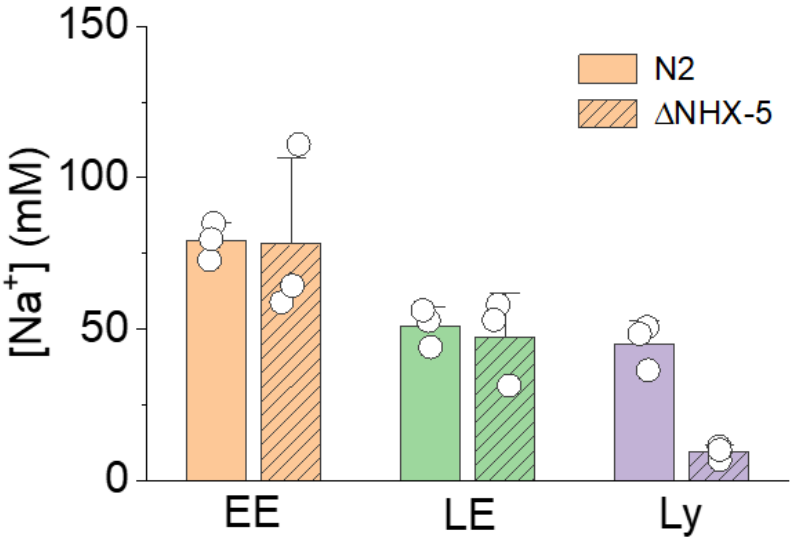

Figure 29. Na+ levels in early endosome, late endosome and lysosomes of N2 and ΔNHX-5 worms. Average luminal Na^+ analysis by compartments. Each data points represents the average lumenal Na^+ of n > 100 endosomes or lysosomes. Note that for the NHX-5 mutant lysosomal Na^+ is significantly and specifically decreased, indicating **Δ**NHX-5 imports Na^+ into the lysosome.

We focused on NHX-5 where lysosomal Na^+ is affected and where adaptability is most impaired.

We measured early endosome and late endosome Na^+ in ΔNHX-5 mutant worms and found that both early endosome and late endosome Na^+ levels are unaltered in adapted worms (Figure 30a). Yet lysosomal Na^+ increased ~8-fold upon adaptation in ΔNHX-5 mutants (Figure 30b) indicating that Na^+ transport specifically in the lysosome is crucial for salt adaptation.

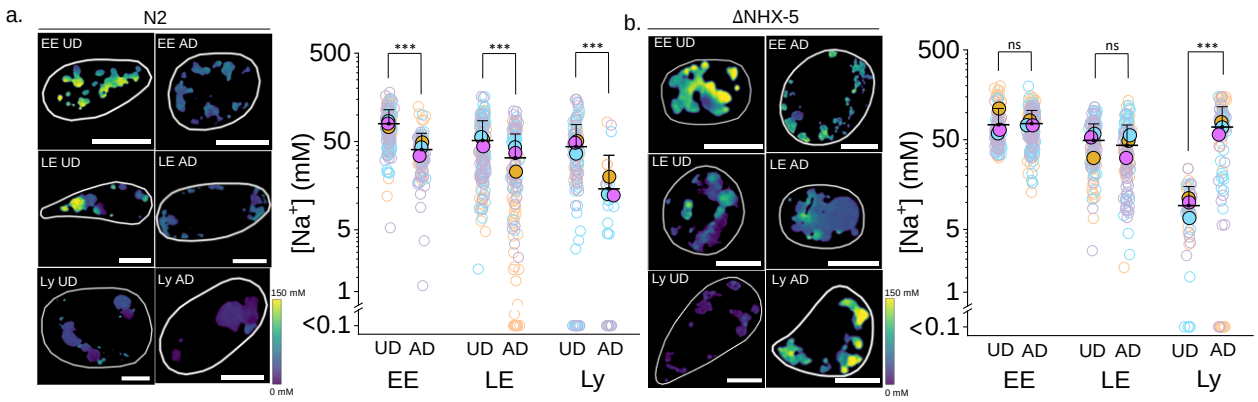

Figure 30. Lysosomal Na^+ transport is crucial for salt adaptation in NHX-5 mutant worms

Single endosome analysis of lumenal Na^+ levels at each stage of the endolysosomal pathway in unadapted (UD) and adapted (AD) N2 (a) and Δnhx-5 (b) worms. Cell is outlined in white. All experiments were performed in triplicate and data from each trial is colour coded. Mean value of each trial is in filled circle of the corresponding colour[83]. *P ≤ 0.05; **P ≤ 0.01; ***P ≤ 0.001; ns, no statistical significance by paired t-test.

Our data shows that the early endosome and the late endosome show comparable Na^+ in NHX-5 mutant and N2 worms (Figure 29). This reveals that under physiological conditions, NHX-5 imports Na^+ specifically in lysosomes. This is the first evidence of a lysosomal Na^+ importer in *C. elegans*. Our data suggests a model where, under salt stress, the increase of Na^+ specifically in lysosomes suggests that NHX-5 changes its direction of transport from one of importing Na^+ to one where Na^+ is exported (Figure 31).

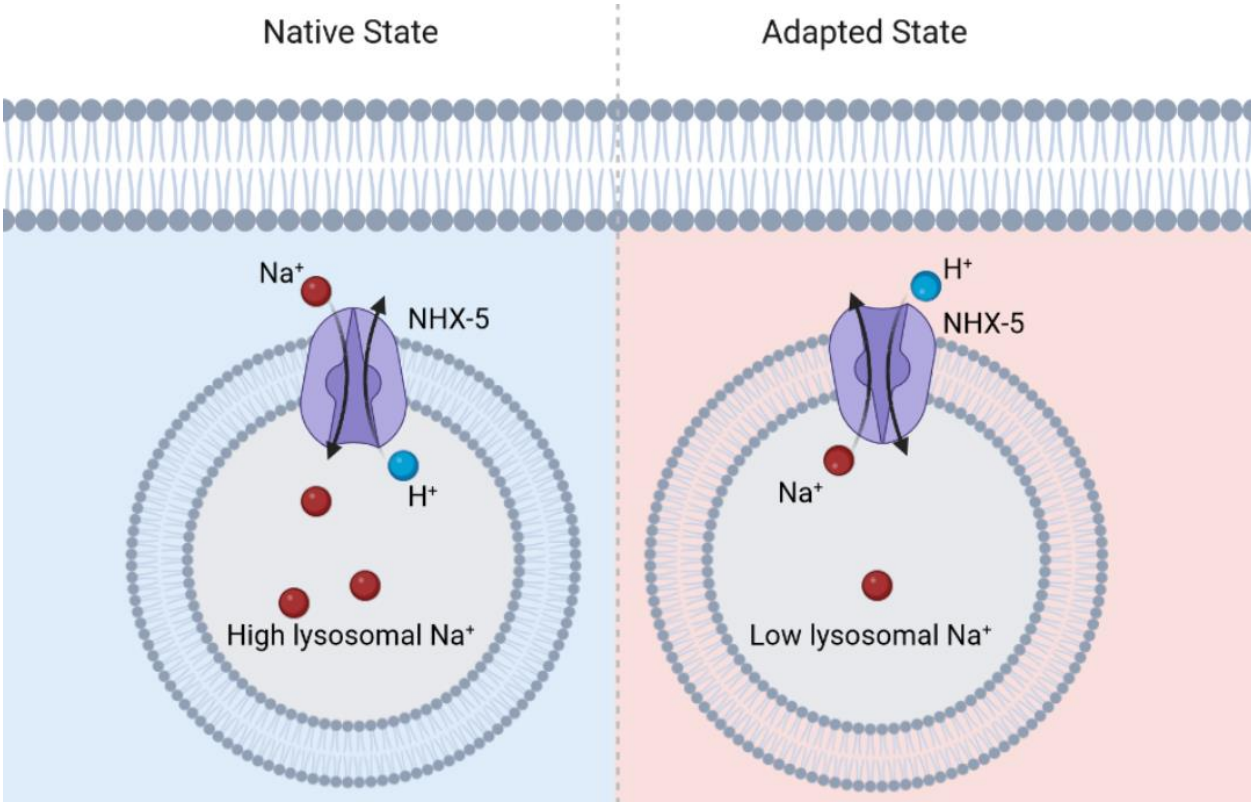

Figure 31. Model of NHX-5 Na^+ transport direction under native state and adapted state

At normal physiology, NHX-5 imports Na^+ to lysosome lumen and help establish Na^+ level of ~40 mM. After adapting to high Na^+, NHX-5 switch its direction of transport to export Na^+, resulting in low Na^+ level of adapted worms. Model created with BioRender.com.

Conclusion

We describe what to our knowledge is the first reporter of organellar Na^+ in live cells and *in vivo*. This reporter technology, denoted *RatiNa*, is ratiometric, pH-insensitive and reports on absolute concentrations of Na^+ in acidic organelles, with single organelle resolution.

Using *RatiNa* we could map lumenal Na^+ levels as a function of endosomal maturation. We found that Na^+ levels decreased progressively along the endolysosomal pathway in *C. elegans*, from ~70 mM in early endosomes to ~40 mM in lysosomes. This contrasts with other previously mapped ions that progressively increase as a function of endosomal maturation. Interestingly, the high Na^+ levels of early endosomes suggests that Na^+ could be a major determinant of the high membrane potential observed in early endosomes.

In lysosomes of both *C. elegans* and mammalian macrophages Na^+ levels proved similar on average. However, single lysosomes in both systems showed considerable variation in terms of their Na^+ levels, ranging from 5 to 150 mM in normal physiological conditions. Our findings resolve the contradictory values obtained previously from bulk or whole cell measurements, which may have led to the upper or lower limits being enriched due to concurrent Na^+ transport [21,79].

Our findings in RAW 264.7 macrophages using the pharmacological inhibition showed that *RatiNa* can map lysosome with perturbed Na^+ level and even diseased state lysosomes. PIKfyve inhibition can influence multiple lysosomal Na^+ transporters but TPC2 should be the main target. CRISPR knockout of TPC2 in RAW macrophages will better prove that TPC2 is responsible for Na^+ efflux in lysosomes.

Interestingly, worms lacking NHX-5, the worm homolog of the human lysosomal Na^+/H^+ exchanger NHE9, showed elevated Na^+. This observation is particularly exciting since this is the first evidence of a *bona fide* lysosomal Na^+ importer in any live system. Lysosomal Na^+ concentration is higher than cytosolic Na^+ concentration and there must be a transporter to establish and maintain such gradient. As an example Na^+/K^+ ATPase on the plasma membrane is necessary to maintain the Na^+ gradient across the plasma membrane[107]. More experiments are required to establish detailed function of NHX-5 such as *in vitro* reconstitution and live labeling for subcellular localization. In addition, NHE9 protein, the human homolog, is also a crucial gene for autism[106,108]. There is an intriguing yet unexplored implication of NHE9 in terms of its Na^+ transporting activity as an autism risk gene. All previous reports have attributes NHE9 as a pH modulator for endosomes and this is the first evidence NHE can also modulate Na^+ level in endosomes and lysosomes[106].

Exchangers are bidirectional and can switch direction for transport when necessary[109], and the direction of ion transport on a given organelle cannot be predicted unless tested. Our studies indicate that NHX5 imports Na^+ into worm lysosomes at normal physiological conditions but switch to export Na^+ in high salt adapted state.

Compared to other organelles, it was the lack of a Na^+ transporter in the lysosome that most impacted the ability of the worm to withstand salt stress. In fact, N2 worms that adapted to salt stress showed far lower Na^+ levels specifically in their lysosomes among all the organelles on the endolysosomal pathway. The trend was opposite for the NHX-5 worms which lysosomal Na+ levels increase specifically, suggesting that lysosome may be the most important organelle in the process of salt adaptation.

Cumulatively, our studies reveal lysosomes as a critical conduit for Na^+ homeostasis in metazoans. Given that vacuoles in yeast are analogous to lysosomes in metazoan cells, our findings are consistent with pioneering studies showing that vacuolar Na^+/H^+ exchangers such as NHX-1 were necessary for yeast survival in high salt conditions[110]. NHX-1 was shown to sequester Na+ in vacuoles and contribute to the maintenance of cytosolic pH and Na^+ levels under salt stress. Even in mammalian cells, lysosomes are key to cells being able to counter osmotic stress, which is inextricably linked to salt stress. For example, lysosome-resident LRRC8, which is part of the volume regulated anion channels (VRAC), is required for cell survival in hypotonic stress[111]. In another instance, lysosome biogenesis is induced by hyperosmotic stress and brought about by NHE7 being delivered to the plasma membrane.[112]

Cellular adaptation upon prolonged exposure to high Na+ is accompanied by numerous metabolic changes that serve to produce inert organic osmolytes such as sorbitol to increase the internal osmotic pressure[113]. These osmolytes are synthesized from energy sources such as glucose[114]. To compensate for the low energy generated by glucose catabolism, cells upregulate autophagy and lysosomal proteolysis[14,15,115]. The upregulation of lysosomal proteolysis and autophagy leads to the activity of numerous nutrient transporters to export and recycle lysosomal degradation products into the cytosol[116]. Nearly half of all known nutrient transporters either leverage the transmembrane lysosomal Na^+ gradient or cotransport Na^+ as they move their substrates across the membrane. For example, the activity of the lysosomal arginine transporter SLC38A9 increases along with lumenal Na^+ levels[28]. Hence one can reconcile the large changes in the steady state levels of lysosomal Na^+ during adaptation to salinity.

While Na^+ homeostasis is extensively studied, its mobilization and metabolism remain unmapped at the sub-cellular level. *RatiNa* is a powerful tool to explore Na^+ metabolism at sub-cellular

resolution in living systems and reveal the contribution of organelles to cellular Na^+ homeostasis. Because so many sub-cellular nutrient transporters use Na^+[117,118], one can potentially map their activity in real-time and *in vivo* by quantitatively imaging organellar Na^+. This new organellar Na^+ reporter technology could be deployed to discover new organellar nutrient transporters, organellar Na^+ channels and transporters[119]. It can also be used in high throughput screens to identify chemical modulators of these organelle-resident proteins and reveal Na^+ homeostasis at an entirely new level of cellular detail[120].

References

1. Hodgkin, A. L. & Huxley, A. F. A quantitative description of membrane current and its application to conduction and excitation in nerve. *J. Physiol.* **117**, 500–544 (1952).
2. Hodgkin, A. L. & Huxley, A. F. The dual effect of membrane potential on sodium conductance in the giant axon of Loligo. *J. Physiol.* **116**, 497–506 (1952).
3. Chatton, J.-Y., Magistretti, P. J. & Barros, L. F. Sodium signaling and astrocyte energy metabolism. *Glia* **64**, 1667–1676 (2016).
4. Adrogué, H. J. & Madias, N. E. Sodium and Potassium in the Pathogenesis of Hypertension. *N. Engl. J. Med.* **356**, 1966–1978 (2007).
5. Erecińska, M. & Silver, I. A. Ions and energy in mammalian brain. *Prog. Neurobiol.* **43**, 37–71 (1994).
6. Kaspari, M. The seventh macronutrient: how sodium shortfall ramifies through populations, food webs and ecosystems. *Ecol. Lett.* **23**, 1153–1168 (2020).
7. Kronzucker, H. J., Coskun, D., Schulze, L. M., Wong, J. R. & Britto, D. T. Sodium as nutrient and toxicant. *Plant Soil* **369**, 1–23 (2013).
8. Haron, H., Hiew, I., Shahar, S., Michael, V. & Ambak, R. A Survey on Salt Content Labeling of the Processed Food Available in Malaysia. *Int. J. Environ. Res. Public. Health* **17**, 2469 (2020).
9. Murphy, E. & Eisner, D. A. Regulation of Intracellular and Mitochondrial Sodium in Health and Disease. *Circ. Res.* **104**, 292–303 (2009).
10. Group, B. M. J. P. Intersalt: an international study of electrolyte excretion and blood pressure. Results for 24 hour urinary sodium and potassium excretion. Intersalt Cooperative Research Group. *Br. Med. J.* **297**, 319–328 (1988).

11. The top 10 causes of death. https://www.who.int/news-room/fact-sheets/detail/the-top-10-causes-of-death.
12. Karppanen, H. & Mervaala, E. Sodium intake and hypertension. *Prog. Cardiovasc. Dis.* **49**, 59–75 (2006).
13. Mente, A. *et al.* Urinary sodium excretion, blood pressure, cardiovascular disease, and mortality: a community-level prospective epidemiological cohort study. *The Lancet* **392**, 496–506 (2018).
14. Skou, J. C. The Identification of the Sodium–Potassium Pump (Nobel Lecture). *Angew. Chem. Int. Ed.* **37**, 2320–2328 (1998).
15. Howarth, C., Gleeson, P. & Attwell, D. Updated energy budgets for neural computation in the neocortex and cerebellum. *J. Cereb. Blood Flow Metab.* **32**, 1222–1232 (2012).
16. Kondapalli, K. C., Prasad, H. & Rao, R. An inside job: how endosomal Na+/H+ exchangers link to autism and neurological disease. *Front. Cell. Neurosci.* **8**, (2014).
17. Bröer, S. The SLC38 family of sodium–amino acid co-transporters. *Pflüg. Arch. - Eur. J. Physiol.* **466**, 155–172 (2014).
18. Shapovalov, G. *et al.* Organelle membrane derived patches: reshaping classical methods for new targets. *Sci. Rep.* **7**, 14082 (2017).
19. Ko, M., Quiñones-Hinojosa, A. & Rao, R. Emerging links between endosomal pH and cancer. *Cancer Metastasis Rev.* **39**, 519–534 (2020).
20. Saminathan, A. *et al.* A DNA-based voltmeter for organelles. *Nat. Nanotechnol.* **16**, 96–103 (2021).
21. Wang, X. *et al.* TPC Proteins Are Phosphoinositide- Activated Sodium-Selective Ion Channels in Endosomes and Lysosomes. *Cell* **151**, 372–383 (2012).

22. Palty, R. *et al.* NCLX is an essential component of mitochondrial Na+/Ca2+ exchange. *Proc. Natl. Acad. Sci.* **107**, 436–441 (2010).
23. Nakamura, N., Tanaka, S., Teko, Y., Mitsui, K. & Kanazawa, H. Four Na+/H+ exchanger isoforms are distributed to Golgi and post-Golgi compartments and are involved in organelle pH regulation. *J. Biol. Chem.* **280**, 1561–1572 (2005).
24. Brett, C. L., Wei, Y., Donowitz, M. & Rao, R. Human Na+/H+ exchanger isoform 6 is found in recycling endosomes of cells, not in mitochondria. *Am. J. Physiol.-Cell Physiol.* **282**, C1031–C1041 (2002).
25. Nass, R., Cunningham, K. W. & Rao, R. Intracellular Sequestration of Sodium by a Novel Na+/H+ Exchanger in Yeast Is Enhanced by Mutations in the Plasma Membrane H+-ATPase: INSIGHTS INTO MECHANISMS OF SODIUM TOLERANCE *. *J. Biol. Chem.* **272**, 26145–26152 (1997).
26. Twig, G. *et al.* Fission and selective fusion govern mitochondrial segregation and elimination by autophagy. *EMBO J.* **27**, 433–446 (2008).
27. Stutzmann, G. E. & Mattson, M. P. Endoplasmic Reticulum Ca2+ Handling in Excitable Cells in Health and Disease. *Pharmacol. Rev.* **63**, 700–727 (2011).
28. Rebsamen, M. *et al.* SLC38A9 is a component of the lysosomal amino acid sensing machinery that controls mTORC1. *Nature* **519**, 477–481 (2015).
29. Xu, H., Ghishan, F. K. & Kiela, P. R. SLC9 Gene Family: Function, Expression, and Regulation. *Compr. Physiol.* **8**, 555–583 (2018).
30. Fukada-Tanaka, S., Inagaki, Y., Yamaguchi, T., Saito, N. & Iida, S. Colour-enhancing protein in blue petals. *Nature* **407**, 581–581 (2000).

31. Lamason, R. L. *et al.* SLC24A5, a Putative Cation Exchanger, Affects Pigmentation in Zebrafish and Humans. *Science* **310**, 1782–1786 (2005).
32. Smith, N. K. & Cameron, I. L. Observations on electron probe x-ray microanalysis compared to other methods for measuring intracellular elemental concentration. *Scan. Electron Microsc.* 395–408 (1981).
33. Aron, A. T., Reeves, A. G. & Chang, C. J. Activity-based sensing fluorescent probes for iron in biological systems. *Curr. Opin. Chem. Biol.* **43**, 113–118 (2018).
34. Greenwald, E. C., Mehta, S. & Zhang, J. Genetically Encoded Fluorescent Biosensors Illuminate the Spatiotemporal Regulation of Signaling Networks. *Chem. Rev.* **118**, 11707–11794 (2018).
35. Suzuki, J., Kanemaru, K. & Iino, M. Genetically Encoded Fluorescent Indicators for Organellar Calcium Imaging. *Biophys. J.* **111**, 1119–1131 (2016).
36. Palmer, A. E., Qin, Y., Park, J. G. & McCombs, J. E. Design and application of genetically encoded biosensors. *Trends Biotechnol.* **29**, 144–152 (2011).
37. Tsien, R. Y. New calcium indicators and buffers with high selectivity against magnesium and protons: design, synthesis, and properties of prototype structures. *Biochemistry* **19**, 2396–2404 (1980).
38. Grimm, J. B., Heckman, L. M. & Lavis, L. D. The chemistry of small-molecule fluorogenic probes. *Prog. Mol. Biol. Transl. Sci.* **113**, 1–34 (2013).
39. Choi, N.-E., Lee, J.-Y., Park, E.-C., Lee, J.-H. & Lee, J. Recent Advances in Organelle-Targeted Fluorescent Probes. *Molecules* **26**, 217 (2021).
40. Modi, S. *et al.* A DNA nanomachine that maps spatial and temporal pH changes inside living cells. *Nat. Nanotechnol.* **4**, 325 (2009).

41. Xu, H., Martinoia, E. & Szabo, I. Organellar channels and transporters. *Cell Calcium* **58**, 1–10 (2015).

42. Modi, S., Nizak, C., Surana, S., Halder, S. & Krishnan, Y. Two DNA nanomachines map pH changes along intersecting endocytic pathways inside the same cell. *Nat. Nanotechnol.* **8**, 459–467 (2013).

43. Saha, S., Prakash, V., Halder, S., Chakraborty, K. & Krishnan, Y. A pH-independent DNA nanodevice for quantifying chloride transport in organelles of living cells. *Nat. Nanotechnol.* **10**, 645–651 (2015).

44. Park, J., Lee, J. & Choi, C. Mitochondrial Network Determines Intracellular ROS Dynamics and Sensitivity to Oxidative Stress through Switching Inter-Mitochondrial Messengers. *PLOS ONE* **6**, e23211 (2011).

45. Chakraborty, K., Veetil, A. T., Jaffrey, S. R. & Krishnan, Y. Nucleic Acid–Based Nanodevices in Biological Imaging. *Annu. Rev. Biochem.* **85**, 349–373 (2016).

46. Kawasaki, T. & Kawai, T. Toll-Like Receptor Signaling Pathways. *Front. Immunol.* **5**, (2014).

47. Kawasaki, T. & Kawai, T. Chapter One - Discrimination Between Self and Non-Self-Nucleic Acids by the Innate Immune System. in *International Review of Cell and Molecular Biology* (eds. Vanpouille-Box, C. & Galluzzi, L.) vol. 344 1–30 (Academic Press, 2019).

48. Veetil, A. T. *et al.* DNA-based fluorescent probes of NOS2 activity in live brains. *Proc. Natl. Acad. Sci. U. S. A.* **117**, 14694–14702 (2020).

49. Proudnikov, D. & Mirzabekov, A. Chemical Methods of DNA and RNA Fluorescent Labeling. *Nucleic Acids Res.* **24**, 4535–4542 (1996).

50. Krishnan, Y., Zou, J. & Jani, M. S. Quantitative Imaging of Biochemistry in Situ and at the Nanoscale. *ACS Cent. Sci.* **6**, 1938–1954 (2020).
51. Pedersen, C. J. Cyclic polyethers and their complexes with metal salts. *J. Am. Chem. Soc.* **89**, 2495–2496 (1967).
52. Minta, A. & Tsien, R. Y. Fluorescent indicators for cytosolic sodium *. *J. Biol. Chem.* **264**, 19449–19457 (1989).
53. Meier, S. D., Kovalchuk, Y. & Rose, C. R. Properties of the new fluorescent Na+ indicator CoroNa Green: Comparison with SBFI and confocal Na+ imaging. *J. Neurosci. Methods* **155**, 251–259 (2006).
54. Kim, M. K. *et al.* Sodium-Ion-Selective Two-Photon Fluorescent Probe for In Vivo Imaging. *Angew. Chem. Int. Ed.* **49**, 364–367 (2010).
55. Schwarze, T., Müller, H., Schmidt, D., Riemer, J. & Holdt, H.-J. Design of Na+-Selective Fluorescent Probes: A Systematic Study of the Na+-Complex Stability and the Na+/K+ Selectivity in Acetonitrile and Water. *Chem. – Eur. J.* **23**, 7255–7263 (2017).
56. Szmacinski, H. & Lakowicz, J. R. Sodium Green as a Potential Probe for Intracellular Sodium Imaging Based on Fluorescence Lifetime. *Anal. Biochem.* **250**, 131–138 (1997).
57. Blakemore, J. D., Chitta, R. & D'Souza, F. Synthesis and study of crown ether-appended boron dipyrrin chemosensors for cation detection. *Tetrahedron Lett.* **48**, 1977–1982 (2007).
58. Kollmannsberger, M., Rurack, K., Resch-Genger, U., Rettig, W. & Daub, J. Design of an efficient charge-transfer processing molecular system containing a weak electron donor: spectroscopic and redox properties and cation-induced fluorescence enhancement. *Chem. Phys. Lett.* **329**, 363–369 (2000).

59. Sarkar, A. R., Heo, C. H., Park, M. Y., Lee, H. W. & Kim, H. M. A small molecule two-photon fluorescent probe for intracellular sodium ions. *Chem. Commun.* **50**, 1309–1312 (2014).

60. Thiagarajah, J. R., Jayaraman, S., Naftalin, R. J. & Verkman, A. S. In vivo fluorescence measurement of Na(+) concentration in the pericryptal space of mouse descending colon. *Am. J. Physiol. Cell Physiol.* **281**, C1898-1903 (2001).

61. Torabi, S.-F. *et al.* In vitro selection of a sodium-specific DNAzyme and its application in intracellular sensing. *Proc. Natl. Acad. Sci.* **112**, 5903–5908 (2015).

62. Gao, G. *et al.* Fluorescent sensors for sodium ions. *Anal. Methods* **9**, 5570–5579 (2017).

63. Luzio, J. P., Pryor, P. R. & Bright, N. A. Lysosomes: fusion and function. *Nat. Rev. Mol. Cell Biol.* **8**, 622–632 (2007).

64. Holmehave, J., Pedersen, S. K., Jensen, H. H. & Ogilby, P. R. Aarhus green: a tetrafluoro-substituted derivative of fluorescein. *Arkivoc* **2015**, 52–64 (2015).

65. Cao, B., Coelho, S., Li, J., Wang, G. & Pertsinidis, A. Volumetric interferometric lattice light-sheet imaging. *Nat. Biotechnol.* **39**, 1385–1393 (2021).

66. Martin, V. V., Rothe, A. & Gee, K. R. Fluorescent metal ion indicators based on benzoannelated crown systems: a green fluorescent indicator for intracellular sodium ions. *Bioorg. Med. Chem. Lett.* **15**, 1851–1855 (2005).

67. Sletten, E. M. & Bertozzi, C. R. Bioorthogonal chemistry: fishing for selectivity in a sea of functionality. *Angew. Chem. Int. Ed Engl.* **48**, 6974–6998 (2009).

68. Goff, C. M., Matchette, M. A., Shabestary, N. & Khazaeli, S. Complexation of caesium and rubidium cations with crown ethers in N,N-dimethylformamide. *Polyhedron* **15**, 3897–3903 (1996).

69. Narayanaswamy, N. *et al.* A pH-correctable, DNA-based fluorescent reporter for organellar calcium. *Nat. Methods* 1 (2018) doi:10.1038/s41592-018-0232-7.

70. Fares, H. & Greenwald, I. Genetic Analysis of Endocytosis in Caenorhabditis elegans: Coelomocyte Uptake Defective Mutants. *Genetics* **159**, 133–145 (2001).

71. Cui, C. *et al.* A lysosome-targeted DNA nanodevice selectively targets macrophages to attenuate tumours. *Nat. Nanotechnol.* **16**, 1394–1402 (2021).

72. Würth, C., Grabolle, M., Pauli, J., Spieles, M. & Resch-Genger, U. Relative and absolute determination of fluorescence quantum yields of transparent samples. *Nat. Protoc.* **8**, 1535–1550 (2013).

73. Chakraborty, K., Leung, K. & Krishnan, Y. High lumenal chloride in the lysosome is critical for lysosome function. *eLife* **6**, e28862 (2017).

74. Surana, S., Bhat, J. M., Koushika, S. P. & Krishnan, Y. An autonomous DNA nanomachine maps spatiotemporal pH changes in a multicellular living organism. *Nat. Commun.* **2**, 340 (2011).

75. Huotari, J. & Helenius, A. Endosome maturation. *EMBO J.* **30**, 3481–3500 (2011).

76. Eskelinen, E.-L. Roles of LAMP-1 and LAMP-2 in lysosome biogenesis and autophagy. *Mol. Aspects Med.* **27**, 495–502 (2006).

77. Sorochkina, A. I. *et al.* N-Terminally Glutamate-Substituted Analogue of Gramicidin A as Protonophore and Selective Mitochondrial Uncoupler. *PLOS ONE* **7**, e41919 (2012).

78. Taciak, B. *et al.* Evaluation of phenotypic and functional stability of RAW 264.7 cell line through serial passages. *PLoS ONE* **13**, e0198943 (2018).

79. Suresh, B. *et al.* Tubular lysosomes harbor active ion gradients and poise macrophages for phagocytosis. *Proc. Natl. Acad. Sci.* **118**, (2021).

80. Trivedi, P. C., Bartlett, J. J. & Pulinilkunnil, T. Lysosomal Biology and Function: Modern View of Cellular Debris Bin. *Cells* **9**, 1131 (2020).

81. Ishiguro, H., Steward, M. C., Lindsay, A. R. & Case, R. M. Accumulation of intracellular HCO3- by Na(+)-HCO3- cotransport in interlobular ducts from guinea-pig pancreas. *J. Physiol.* **495**, 169–178 (1996).

82. Steinberg, B. E. *et al.* A cation counterflux supports lysosomal acidification. *J. Cell Biol.* **189**, 1171–1186 (2010).

83. Lord, S. J., Velle, K. B., Mullins, R. D. & Fritz-Laylin, L. K. SuperPlots: Communicating reproducibility and variability in cell biology. *J. Cell Biol.* **219**, e202001064 (2020).

84. Prakash, V. *et al.* Quantitative Mapping of Endosomal DNA Processing by Single Molecule Counting. *Angew Chem Int Ed* 20 (2019).

85. Dan, K., Veetil, A. T., Chakraborty, K. & Krishnan, Y. DNA nanodevices map enzymatic activity in organelles. *Nat. Nanotechnol.* **14**, 252–259 (2019).

86. Jani, M. S., Zou, J., Veetil, A. T. & Krishnan, Y. A DNA-based fluorescent probe maps NOS3 activity with subcellular spatial resolution. *Nat. Chem. Biol.* **16**, 660–666 (2020).

87. Thekkan, S. *et al.* A DNA-based fluorescent reporter maps HOCl production in the maturing phagosome. *Nat. Chem. Biol.* **15**, 1165–1172 (2019).

88. Calcraft, P. J. *et al.* NAADP mobilizes calcium from acidic organelles through two-pore channels. *Nature* **459**, 596–600 (2009).

89. Sakurai, Y. *et al.* Two-pore channels control Ebola virus host cell entry and are drug targets for disease treatment. *Science* **347**, 995–998 (2015).

90. Zhang, X. *et al.* Agonist-specific voltage-dependent gating of lysosomal two-pore Na+ channels. *eLife* **8**, e51423.

91. Penny, C. J. *et al.* Mining of Ebola virus entry inhibitors identifies approved drugs as two-pore channel pore blockers. *Biochim. Biophys. Acta Mol. Cell Res.* **1866**, 1151–1161 (2019).
92. Gerndt, S. *et al.* Agonist-mediated switching of ion selectivity in TPC2 differentially promotes lysosomal function. *eLife* **9**, e54712 (2020).
93. Zolov, S. N. *et al.* In vivo, Pikfyve generates PI(3,5)P2, which serves as both a signaling lipid and the major precursor for PI5P. *Proc. Natl. Acad. Sci.* **109**, 17472–17477 (2012).
94. Du, C., Guan, X. & Yan, J. Two-pore channel blockade by phosphoinositide kinase inhibitors YM201636 and PI-103 determined by a histidine residue near pore-entrance. *Commun. Biol.* **5**, 1–11 (2022).
95. Kang, Y.-L. *et al.* Inhibition of PIKfyve kinase prevents infection by Zaire ebolavirus and SARS-CoV-2. *Proc. Natl. Acad. Sci.* **117**, 20803–20813 (2020).
96. Choy, C. H. *et al.* Lysosome enlargement during inhibition of the lipid kinase PIKfyve proceeds through lysosome coalescence. *J. Cell Sci.* **131**, jcs213587 (2018).
97. Dong, X. *et al.* PI(3,5)P_2 controls membrane trafficking by direct activation of mucolipin Ca^{2+} release channels in the endolysosome. *Nat. Commun.* **1**, 38 (2010).
98. Bargmann, C. I. & Horvitz, H. R. Chemosensory neurons with overlapping functions direct chemotaxis to multiple chemicals in C. elegans. *Neuron* **7**, 729–742 (1991).
99. Chatzigeorgiou, M., Bang, S., Hwang, S. W. & Schafer, W. R. tmc-1 encodes a sodium-sensitive channel required for salt chemosensation in C. elegans. *Nature* **494**, 95–99 (2013).
100. Lamitina, S. T., Morrison, R., Moeckel, G. W. & Strange, K. Adaptation of the nematode Caenorhabditis elegans to extreme osmotic stress. *Am. J. Physiol.-Cell Physiol.* **286**, C785–C791 (2004).

101. Choe, K. & Strange, K. Evolutionarily conserved WNK and Ste20 kinases are essential for acute volume recovery and survival following hypertonic shrinkage in Caenorhabditis elegans. *Am. J. Physiol.-Cell Physiol.* (2007) doi:10.1152/ajpcell.00126.2007.

102. Zagórska, A. *et al.* Regulation of activity and localization of the WNK1 protein kinase by hyperosmotic stress. *J. Cell Biol.* **176**, 89–100 (2007).

103. Yang, Y. & Guo, Y. Unraveling salt stress signaling in plants. *J. Integr. Plant Biol.* **60**, 796–804 (2018).

104. Nehrke, K. & Melvin, J. E. The NHX Family of Na+-H+ Exchangers in Caenorhabditis elegans *. *J. Biol. Chem.* **277**, 29036–29044 (2002).

105. Sharma, V. *et al.* Insight into the Family of Na+/Ca2+ Exchangers of Caenorhabditis elegans. *Genetics* **195**, 611–619 (2013).

106. Kondapalli, K. C. *et al.* Functional evaluation of autism-associated mutations in NHE9. *Nat. Commun.* **4**, 2510 (2013).

107. Chibalin, A. V., Katz, A. I., Berggren, P. O. & Bertorello, A. M. Receptor-mediated inhibition of renal Na(+)-K(+)-ATPase is associated with endocytosis of its alpha- and beta-subunits. *Am. J. Physiol.* **273**, C1458-1465 (1997).

108. Morrow, E. M. *et al.* Identifying autism loci and genes by tracing recent shared ancestry. *Science* **321**, 218–223 (2008).

109. Mager, T., Rimon, A., Padan, E. & Fendler, K. Transport Mechanism and pH Regulation of the Na+/H+ Antiporter NhaA from Escherichia coli. *J. Biol. Chem.* **286**, 23570–23581 (2011).

110. Nass, R., Cunningham, K. W. & Rao, R. Intracellular Sequestration of Sodium by a Novel Na+/H+ Exchanger in Yeast Is Enhanced by Mutations in the Plasma Membrane H+-

ATPase: INSIGHTS INTO MECHANISMS OF SODIUM TOLERANCE *. *J. Biol. Chem.* **272**, 26145–26152 (1997).

111. Li, P. *et al.* LRRC8 family proteins within lysosomes regulate cellular osmoregulation and enhance cell survival to multiple physiological stresses. *Proc. Natl. Acad. Sci.* **117**, 29155–29165 (2020).

112. López-Hernández, T., Puchkov, D., Krause, E., Maritzen, T. & Haucke, V. Endocytic regulation of cellular ion homeostasis controls lysosome biogenesis. *Nat. Cell Biol.* **22**, 815–827 (2020).

113. Burg, M. B., Ferraris, J. D. & Dmitrieva, N. I. Cellular Response to Hyperosmotic Stresses. *Physiol. Rev.* **87**, 1441–1474 (2007).

114. Jeffery, J. & Jörnvall, H. Enzyme relationships in a sorbitol pathway that bypasses glycolysis and pentose phosphates in glucose metabolism. *Proc. Natl. Acad. Sci.* **80**, 901–905 (1983).

115. Galluzzi, L., Pietrocola, F., Levine, B. & Kroemer, G. Metabolic Control of Autophagy. *Cell* **159**, 1263–1276 (2014).

116. Wang, W. *et al.* Up-regulation of lysosomal TRPML1 channels is essential for lysosomal adaptation to nutrient starvation. *Proc. Natl. Acad. Sci.* **112**, E1373–E1381 (2015).

117. Verdon, Q. *et al.* SNAT7 is the primary lysosomal glutamine exporter required for extracellular protein-dependent growth of cancer cells. *Proc. Natl. Acad. Sci. U. S. A.* **114**, E3602–E3611 (2017).

118. Wyant, G. A. *et al.* mTORC1 Activator SLC38A9 Is Required to Efflux Essential Amino Acids from Lysosomes and Use Protein as a Nutrient. *Cell* **171**, 642-654.e12 (2017).

119. Narayanaswamy, N. *et al.* A pH-correctable, DNA-based fluorescent reporter for organellar calcium. *Nat. Methods* **16**, 95–102 (2019).

120. Tay, B., Stewart, T. A., Davis, F. M., Deuis, J. R. & Vetter, I. Development of a high-throughput fluorescent no-wash sodium influx assay. *PLOS ONE* **14**, e0213751 (2019).